An inter-organ neural circuit for appetite suppression

Tong Zhang[1,4,5], **Matthew H. Perkins**[1], **Hao Chang**[1], **Wenfei Han**[1,*], **Ivan E. de Araujo**[1,2,3,6,*]

[1]Nash Family Department of Neuroscience, Icahn School of Medicine at Mount Sinai, New York City, NY 10029, USA

[2]Artificial Intelligence and Emerging Technologies in Medicine, Icahn School of Medicine at Mount Sinai, New York City, NY 10029, USA

[3]Diabetes, Obesity and Metabolism Institute, Icahn School of Medicine at Mount Sinai, New York City, NY 10029, USA

[4]Department of Colorectal Surgery, Guangzhou First People's Hospital, South China University of Technology, Guangzhou, Guangdong 510180, China

[5]Jinan University, Guangzhou, Guangdong 510632, China

[6]Lead contact

SUMMARY

Glucagon-like peptide-1 (GLP-1) is a signal peptide released from enteroendocrine cells of the lower intestine. GLP-1 exerts anorectic and antimotility actions that protect the body against nutrient malabsorption. However, little is known about how intestinal GLP-1 affects distant organs despite rapid enzymatic inactivation. We show that intestinal GLP-1 inhibits gastric emptying and eating via intestinofugal neurons, a subclass of myenteric neurons that project to abdominal sympathetic ganglia. Remarkably, cell-specific ablation of intestinofugal neurons eliminated intestinal GLP-1 effects, and their chemical activation functioned as a GLP-1 mimetic. GLP-1 sensing by intestinofugal neurons then engaged a sympatho-gastro-spinal-reticular-hypothalamic pathway that links abnormal stomach distension to craniofacial programs for food rejection. Within this pathway, cell-specific activation of discrete neuronal populations caused systemic GLP-1-like effects. These molecularly identified, delimited enteric circuits may be targeted to ameliorate the abdominal bloating and loss of appetite typical of gastric motility disorders.

In brief

*Correspondence: wenfei.han@mssm.edu (W.H.), ivan.dearaujo@mssm.edu (I.E.d.A.).

Local actions of the gut peptide GLP-1 are sufficient to cause marked gastric distension and appetite suppression. GLP-1-sensitive ileal neurons connect via abdominal sympathetic ganglia to gastric enteric neurons that cause stomach distension, and stomach volume information is conveyed by the spinal cord to hypothalamic neurons that mediate food rejection.

Graphical Abstract
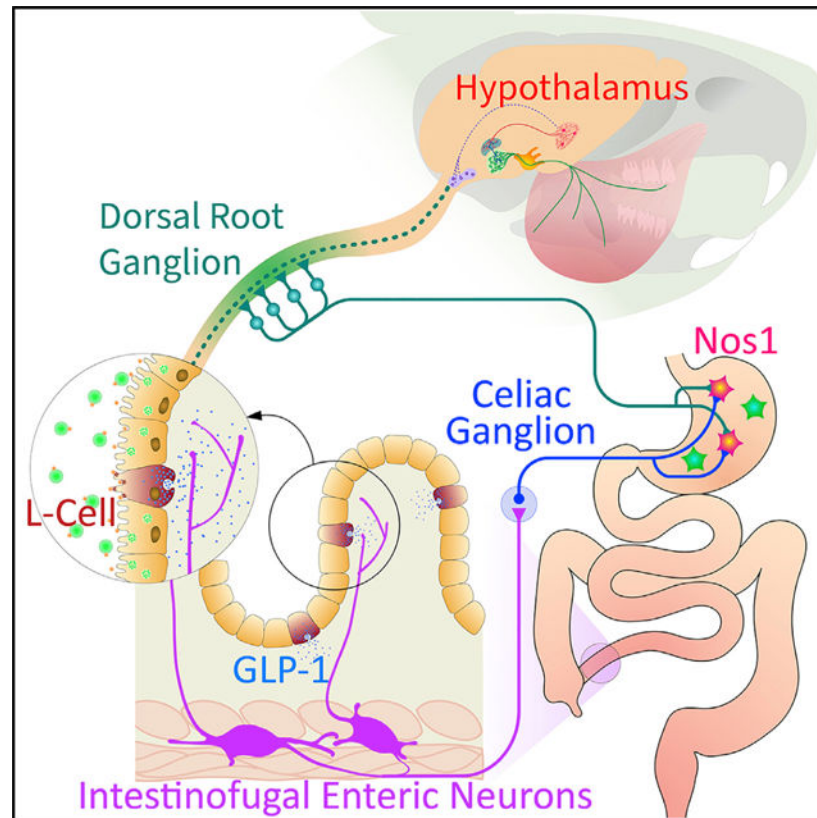
INTRODUCTION

Proglucagon-derived glucagon-like peptide-1 (GLP-1) is an intestinal signal peptide secreted from enteroendocrine L cells of the lower intestine (Dailey and Moran, 2013; Holst, 2007; Müller et al., 2019; Schirra and Göke, 2005). Synthetic GLP-1 analogs, which act as agonists of the GLP-1 receptor, are widely used to control appetite and glucose excursions in overweight individuals (Drucker, 2018). When exogenously administered, GLP-1 potently inhibits food intake and delays gastric emptying by inducing the relaxation of the gastric fundus (Drucker, 2018; Schirra and Göke, 2005). Under physiological conditions, gut-derived GLP-1 secretion is stimulated by direct contact of luminal nutrients with L cells (Herrmann-Rinke et al., 1995; Layer et al., 1995; Ritzel et al., 1997). Critically, most L cells reside in the non-absorptive parts of the lower intestine (Eissele et al., 1992; Holst, 2007; Panaro et al., 2020; Paternoster and Falasca, 2018). Thus, GLP-1 acts to protect the body against malabsorption by inhibiting upper gastrointestinal transit and by inducing anorectic

perceptions such as fullness and discomfort (Plamboeck et al., 2013; Schirra and Göke, 2005).

Although it has been generally assumed that endogenous GLP-1 is an endocrine hormone, this concept appears to be problematic (Burcelin et al., 2009; D'Alessio, 2016). Unlike its synthetic analogs, endogenous GLP-1 is very rapidly inactivated by the ubiquitous enzyme dipeptidyl peptidase-4 in intestinal capillaries and the liver (Deacon, 2005; Hansen et al., 1999). Thus, most of secreted GLP-1 is inactivated before it leaves the gut (Holst et al., 2022), with only a minor fraction remaining intact by the time it reaches arterial circulation (D'Alessio, 2016). Indeed, postprandial rises in plasma GLP-1 are very modest in humans (Vilsbøll et al., 2001), consistent with experiments in rodents that argue against a role for systemic increases in endogenous GLP-1 in satiation (Punjabi et al., 2011). Altogether, these results indicate that endogenous GLP-1 primarily acts locally before rapid degradation (Vahl et al., 2007).

Unfortunately, the peripheral mechanisms of endogenous GLP-1 action remain unclear (Burmeister et al., 2017; Drucker, 2018; Kim et al., 2009; Schirra and Göke, 2005). One distinct possibility is that gut enteric neurons mediate the systemic effects of intestinal GLP-1 (Burcelin et al., 2009; Holst et al., 2022). Accordingly, here we test the hypothesis that intestinal GLP-1 triggers gut-brain neural transmission by recruiting local enteric circuitries. Our rationale is that enteric neurons engaged by intestinal GLP-1 may be targeted to alleviate the anorexia and abdominal bloating typical of motility disorders such as gastroparesis and irritable bowel syndrome (Tack et al., 2006).

RESULTS

Cell-specific activation of ileal L cells causes gastric distention and appetite loss

GLP-1 effects are traditionally studied via either systemic or brain injections. Our aim is to model intestinal GLP-1 secretion by ileal L cells (L^{Cells}). To optogenetically activate L^{Cells} *in vivo*, Gcg^{iCre} mice were crossed to mice expressing a Cre-inducible channelrhodopsin-2/EYFP fusion protein (Ai32 mice). In Gcg^{iCre}×Ai32 mice, a blue laser beam was directed to the terminal ileum via an implanted glass window (see the descriptive table with details for all surgical procedures in STAR Methods). Laser stimulation of L^{Cells} resulted in (~100%) enlargements of gastric volumes (Figures 1A, S1A, and S1B). Laser stimulation also heightened neuronal activity in GLP-1 receptor (GLP-1R)-expressing ileal myenteric neurons (Figures S1C and S1D). We then employed chemogenetic approaches (Sternson and Roth, 2014) to perform behavioral assays upon L^{Cell} stimulation. Gcg^{iCre} mice were crossed to CAG-LSL-Gq mice, allowing *Cre*-inducible expression of the HA-hM3Dq-pta-mCitrine in L^{Cells}. An ileal catheter was implanted in Gcg^{iCre}×CAG-LSL-Gq mice, through which the designer drug clozapine-*N*-oxide (CNO) was infused (5 mg/kg, 50 μL over 10 s for all intra-intestinal infusions). Again, chemical stimulation of L^{Cells} resulted in equally pronounced (~100%) enlargements of gastric volumes. Importantly, this effect was not observed after equivalent intra-peritoneal injections (Figure 1B). Ileal CNO injections also resulted in (~50% of baseline) appetite loss (Figure 1C). Gastric distention and anorexia were blocked by ileal infusions of the GLP-1R antagonist Exendin9–39 (Figures 1B and 1C), implying that secretion of GLP-1 by L^{Cells} is required for these effects.

GLP-1 signaling in terminal ileum is sufficient to inhibit gastric motility and appetite

To approximate the localization and dynamics of GLP-1 release by L[Cells], we implanted a catheter in the lower ileum of mice to perform luminal intra-ileal GLP-1 infusions (GLP-1[ii], 20–25 pmol/kg, 50 μL over 10 s for all intra-intestinal infusions; see STAR Methods and Jessen et al., 2012; Paternoster and Falasca, 2018). GLP-1[ii] was sufficient to induce ~100% enlargements in gastric volume concomitantly to reducing eating to ~50% of baseline in food-restricted mice (Figures 1D and 1E). Baseline plasma glucose levels remained unaffected (Figure S1E). Indeed, GLP-1[ii] primarily impacted gastric motility since electromyograms from awake mice showed reductions in stomach contractions (Figure 1F). Importantly, neither gastric nor feeding effects were detected after intra-peritoneal GLP-1 injections (Figures 1G and 1H). Although equivalent intra-cerebroventricular GLP-1 (GLP-1[icv]) did inhibit eating, they failed to affect gastric volume (Figures 1I and 1J). Local infusion of exendin9–39 into ileum abolished GLP-1[ii] effects (Figure S1F), demonstrating the dependency of GLP-1[ii] on local GLP-1R signaling. Moreover, ileal infusions of bile acids, potent GLP-1 secretagogues (Lund et al., 2020), recapitulated the GLP-1R-dependent effects of both GLP-1[ii] and L[Cell] stimulation (Figures S1G–S1J). Finally, using FRET imaging (Jares-Erijman and Jovin, 2003), we detected GLP-1 signals in the submucosa layers of ileum innervated by processes arising from GLP-1R+ myenteric neurons (Figures 1K, 1L, S1K, and S1L). We conclude that GLP-1 signaling generates site-specific physiological effects.

Effects of ileal GLP-1 are mediated by intestinal, not brainstem, GLP-1 receptors

Consistent with such a key role for ileal GLP-1 receptors, most ileal myenteric neurons responsive to GLP-1[ii] expressed GLP-1Rs (Figures 1M and S1M), and intravital measurements of calcium transients in Glp1r-ires-Cre×Ai148D mice implanted with the abdominal window confirmed the robust responsivity (~89%) of ileal myenteric GLP-1R+ neurons to GLP-1[ii] (Figure 1N). In contrast, and unlike GLP-1[icv], GLP-1[ii] failed to activate GLP-1R+ neurons in the *area postrema* (Figures S1N–S1Q). Next, we ablated ileal GLP-1Rs by locally injecting diphtheria toxin (DT) into the terminal ileum of the Glp1r-ires-Cre × iDTR mice. This eliminated the dose-dependent gastric, neuronal, and anorectic effects of GLP-1[ii] (Figures 1O, 1P, S1R, and S1S). In contrast, eliminating the GLP-1R+ neurons in the *area postrema* did not impact GLP-1[ii] actions (Figures S1T and S1U). Thus, local GLP-1Rs are obligatory mediators of the systemic effects induced by ileal L[Cells].

Cell-specific activation of ileal GLP-1R-expressing myenteric neurons causes gastric distention and appetite loss

We injected the *Cre*-dependent, excitatory chemogenetic construct AAVdj-DIO-Gs-mCherry into the ileum of Glp1r-ires-Cre mice to activate GLP-1R+ enteric neurons. The injections of CNO recapitulated the gastric, anorectic, and central effects of GLP-1[ii] (Figures 1Q, 1R, and S1V).

Ileal intestinofugal myenteric neurons express GLP-1R and mimic ileal GLP-1 actions when chemically activated

Systemic GLP-1 injections activate abdominal sympathetic ganglia in mice (Muller et al., 2020). We found that chemogenetic stimulation of GLP-1R+ enteric neurons was sufficient to induce *c-fos* protein (Fos) expression in abdominal sympathetic celiac ganglia (CG, Figures 2A and S2). Critically, we observed the strong expression of mCherry-positive terminal fibers in CG, in close apposition to Fos+ neurons (i.e., terminals arising from ileal GLP-1R+ neurons transfected with the chemogenetic construct AAVdj-DIO-Gs-mCherry; Figures 2B, S2A, and S2B). We hypothesized that ileal GLP-1+ neurons are intestinofugal (IFN; i.e., myenteric neurons that project to abdominal sympathetic ganglia; Furness, 2006; Hibberd et al., 2020; Szurszewski et al., 2002). Upon injecting the retrograde adeno-associated virus AAVrg-EGFP into CG, we observed that IFNs invariably expressed GLP-1Rs (Figures 2C, 2D, S2C, and S2D). RNA expression analyses also confirmed that IFNs are enriched in *Glp-1r* expression (Figure 2E).

To cell-specifically ablate IFNs, we injected the retrograde, *Cre*-expressing virus AAVrg-EGFP-Cre in the celiac ganglia (CG) of iDTR mice. Ileal DT injections eliminated the gastric, anorectic, as well as the CG and brain effects induced by GLP-1[ii]; moreover, this treatment equally suppressed GLP-1R expression in the ileal, but not jejunal, myenteric layer (Figures 2F–2I and S2E–S2J). Of note, IFN ablation was sufficient to abolish gastric distension induced by intra-peritoneal injections of the GLP-1R agonist Exendin-4 (Figure S2K). This implies that systemic GLP-1 drugs also engage GLP-1R+ ileal myenteric neurons to reduce gut motility.

To cell-specifically activate IFNs, we once again injected AAV2-retro-hSyn.HI.eGFP-Cre in CG, followed by *Cre*-dependent AAVdj—DIO-Gs-mCherry into the ileum of wild-type mice. CNO injections closely mimicked the neuronal and appetitereducing effects of GLP-1[ii] (Figures 2J–2M and S2L–S2N). Of note, ablating CG neurons via injections into CG of the *Cre*-induced caspase3 construct AAV-flex-Casp3 abolished the effects of IFN chemical activation (see Figure 2L), implying that IFNs engage CG to transduce ileal GLP-1 signals. In sum, ileal IFNs are necessary and sufficient for the gastric and feeding effects produced by local GLP-1 release.

The ileal brake reflex is mediated by intestinofugal neurons

The "ileal brake" refers to the phenomenon by which the presence of nutrients or bile within the distal intestine triggers an intestino-gastric feedback loop that inhibits upper gut motility and appetite (thereby preventing nutrient malabsorption; Read et al., 1984; Schirra and Göke, 2005). Intestinal GLP-1 has been implicated in this defensive mechanism (Giralt and Vergara, 1999; Schirra and Göke, 2005). We therefore hypothesized that IFN inhibition would disrupt the ileal brake reflex. To inhibit IFNs, we once again injected AAVrg-EGFP-Cre in CG followed by injections in the ileum of the *Cre*-dependent inhibitory designer receptor construct AAVdj-DIO-Gi-mCherry. Chemogenetic inhibition of IFNs abolished the anorectic effects of ileal lipid infusions (Figures 2N–2P and S2O–S2Q), recapitulating the effects of exendin9–39 to the ileum. These studies implicate IFNs as key mediators of the ileal brake reflex.

Intestinal GLP-1 controls the stomach via abdominal sympathetic ganglia

Using cells-specific anatomical, chemogenetic, and ablation approaches, we established that IFNs act on the stomach by recruiting stomach-innervating noradrenergic CG neurons (henceforth CG$^{NA–Stom}$; for details, see ileal-stomach connectivity via abdominal sympathetic ganglia section in STAR Methods). These studies are shown in Figures 3 and S3.

Intestinal GLP-1 controls appetite and stomach distension via nitric oxide gastric neurons

We hypothesized that inhibitory gastric neuronal mechanisms operate downstream of the L^{Cell} → IFN^{Stom} → CG$^{NA–Stom}$ circuitry. The stomach contains neurons expressing either neuronal nitric oxide (Nos1) or choline acetyltransferase (ChAT), respectively the main inhibitory and excitatory markers for gut motor neurons (Furness et al., 2014). Since sympathetic tone inhibits gut motility, we tested the hypothesis that Nos1+ gastric neurons (henceforth Nos1^{Stom}) are the preferential targets of CG$^{NA–Stom}$. To visualize CG^{Stom} targets, we injected AAVrg-EGFP-Cre into the muscle layers of the stomach body, followed by injections of the *herpes simplex* strain HSV-LSL-TK-tdTomato (Lo and Anderson, 2011) into CG. Herpes-infected neurons were predominantly Nos1^{Stom} (Figures 4A, 4B, and S4A). In contrast, similar injections into the parasympathetic dorsal motor nucleus of the vagus (DMV) infected predominantly ChAT+ neurons (henceforth ChAT^{Stom}; Figure S4B). Consistently, we observed dense labeling in CG (and sensory ganglia) upon rabies SAD-DG-GFP injections into the stomach of Nos1^{cre} but not of ChAT-IRES-Cre mice (Figures 4C, 4D, and S4A–S4C). Thus, CG^{Stom} preferentially and densely target Nos1^{Stom}.

In vivo, GLP-1^{ii} caused preferential Fos expression in Nos1^{Stom}, an effect abolished by the ablation of CG$^{NA–Stom}$ with DβH–saporin, a compound that acts to specifically ablate noradrenaline cells via retrograde uptake (Milstein et al., 2007) (Figures 4E, 4F, and S4D). Moreover, cell-specific intravital imaging of Nos1^{cre} mice showed that ~44% of Nos1^{Stom} were activated by GLP-1^{ii} (Figure 4G). In contrast, only ~16% of ChAT^{Stom} were activated by GLP-1^{ii} (Figure 4H).

We therefore predicted that Nos1^{Stom} are critical for the bloating and anorectic effects of GLP-1^{ii}. We cell-specifically ablated Nos1^{Stom} by injecting the *Cre*-inducible caspase3 construct AAV1-flex-Casp3 into the body of the stomach of Nos1^{cre} mice. This manipulation abolished both the gastric distension, central, and anorexia effects induced by GLP-1^{ii} (Figures 4I, 4J, and S4E).

Gastroparesis and anorexia induced by truncal vagotomy are abolished by ablation of nitric oxide gastric neurons

To confirm this mechanism, we assessed the effects of gastric Nos1^{Stom} ablation on truncal vagotomies, a treatment that equally causes gastroparesis and anorexia. Strikingly, Nos1^{Stom} ablation abolished truncal vagotomy-induced gastric paresis and distension (Figure 4K). Moreover, Nos1^{Stom} ablation normalized feeding and weight gain parameters in vagotomized mice (Figures S4F and S4G; Video S1). Thus, Nos1^{Stom} emerge as obligatory components of the gut circuitry that mediates distension-induced anorexia, including upon gut GLP-1 or vagotomy.

Chemical activation of nitric oxide gastric neurons mimics intestinal GLP-1

We next hypothesized that the chemogenetic activation of Nos1^{Stom} would mimic GLP-1^{ii} and L^{Cell} activation. We injected the *Cre*-dependent excitatory designer construct AAVdj-DIO-Gs-mCherry into the stomach of Nos1^{cre} mice. We found that CNO injections strongly inhibited gastric contractions (Figure 4L), caused marked gastric distension (Figure 4M), and reduced eating to ~50% of baseline levels (Figures 4N, S4H, and S4I), i.e., *in vivo* effects that mirror those obtained with GLP-1^{ii} and L^{Cell} activation.

Activation of cholinergic gastric neurons antagonizes the effects of intestinal GLP-1 and stomach bloating

We next predicted symmetrical effects upon performing the same manipulations on excitatory ChAT^{Stom}. AAVdj-DIO-GsmCherry was injected into the stomach of ChAT-IRES-Cre mice. Although ChAT^{Stom} activation did not significantly increased stomach contractions (Figure 4O), it did abolish both the distension, anorectic, and neuronal effects of GLP-1^{ii} (Figures 4P, 4Q, and S4J). To confirm that ChAT^{Stom} activation is sufficient to counteract gastric distension, we implanted an intra-gastric balloon in ChAT-IRES-Cre mice to mimic the gastric bloating effects of GLP-1^{ii}. Although balloon inflation strongly inhibited eating, this effect was entirely abolished by ChAT^{Stom} activation (Figures 4R–4T and S4K–S4N).

Accordingly, we next predicted that ablating ChAT^{Stom} would mimic the distension and anorectic effects of GLP-1^{ii}. We then injected the caspase3 construct AAV5-flex-taCasp3 into the stomach of ChAT-IRES-Cre mice, which resulted in dramatic gastric distension and ensuing starvation (Figures 4U, S4O, and S4P). These effects were not influenced by celiactomies (as expected, since CG^{Stom} does not innervate ChAT^{Stom}; Figure S4O). Overall, these findings show that gastric distension is an essential mediator of the anorectic actions of intestinal GLP-1, as induced via the L^{Cell}→IFN^{Stom}→CG$^{NA–Stom}$→Nos1^{Stom} circuitry.

GLP-1-induced gastric distension signals are transmitted to the brain via spinal, not vagal, sensory neurons

We next aimed at characterizing how GLP-1-induced distension signals may be transmitted to the brain. Both vagal and spinal sensory ganglia innervate the gut and play a role in systemic GLP-1 analog signaling (Borgmann et al., 2021). We thus performed organ-specific sensory ablations of either the vagal or spinal innervation of the stomach. We injected the retrograde, Cre-expressing AAVrg-EGFP-Cre virus into the muscle layers of the stomach of iDTR mice followed by injections of DT either intrathecally (to target stomach-innervating DRGs, DRG^{Stom}) or into the vagal nodose ganglia (to target stomach-innervating nodose neurons, NG^{Stom}).

DRG^{Stom} ablation was sufficient to abolish appetite suppression induced by GLP-1^{ii} (Figure 5A). To confirm that these effects derive from sensing gastric distension, we performed additional experiments using intra-gastric balloons. Although control animals ate only ~10% of their normal meal size when the balloon was inflated, DRG^{Stom} animals ate about ~70%

of their normal meal size (i.e., DRG^{Stom} animals were ~7 times less sensitive to balloon distension; Figure 5B).

In contrast, NG^{Stom} ablation failed to affect appetite suppression induced by GLP-1^{ii} (Figure 5C). Similarly, intra-gastric balloon experiments revealed that appetite loss was not affected by vagal sensory denervation (Figure 5D). We confirmed these results by injecting NG with cholecystokinin-conjugated saporin, a neurotoxin that specifically ablates gut-innervating NG neurons (Han and de Araujo, 2021). This treatment also failed to prevent balloon inflation-induced anorexia (Figures S5A–S5H). Thus, DRG^{Stom}, but not NG^{Stom}, appear essential for brain sensing of GLP-1-induced gastric distension via a L^{Cell}→IFN^{Stom}→CG$^{NA–Stom}$→Nos1^{Stom}→DRG^{Stom} pathway.

Spinal sensory ganglia transmit gastric information to the parasubthalamic nucleus of the lateral hypothalamus via the medullary reticular formation

Finally, we set to determine the pathways via which DRG^{Stom} signals distension to the brain and how appetite suppression is executed. Accordingly, we performed a series of anatomical, electrophysiological, optogenetic, and lesion studies (for details on the approach, see anatomical, electrophysiological, lesion, and optogenetic studies linking spinal transmission from stomach to brain section in STAR Methods). We found that the lateral reticular formation (LRN), a medullary nucleus involved in decoding proprioceptive spinal signals (Pivetta et al., 2014), anatomically links DRG^{Stom} to the parasubthalamic nucleus (PSTn; Barbier et al., 2020), a lateral hypothalamic region involved in appetite suppression (Figures 5E, 5F, 6A, S5I–S5O, and S6A; Table S1). A sizable proportion of LRN neurons displayed rapid modulatory changes in firing rates in response to gastric contraction events (Figures 6B–6M and S6B–S6K). LRN is therefore a relay node within an interconnected network linking ileal GLP-1R+ neurons to PSTn VGlut2+ neurons (PSTn^{VGlut2}; Figures 7Aa–7Ag). Consistently, PSTn neurons responded to intestinal GLP-1 (Figures 7B–7J, S7A, and S7B) and encoded for gastric distension volumes (Figures 7K–7O, and S7C). Finally, PSTn^{VGlut2} neurons are required for the anorectic effects of GLP-1^{ii} (Figure 7P) and, via projections to craniofacial musculatures, control motor programs for food rejection (Figures 7Q–7HH and S7D–S7P; Videos S2 and S3).

DISCUSSION

We delineated a novel gut-brain sensorimotor circuit, L^{Cell}→IFN^{Stom}→CG$^{NA–Stom}$→Nos1^{Stom}→DRG^{Stom}→LRN^{T-DRG}→PSTn^{VGlut2}→PCRt→Jaw. This circuit forms an inter-organ neural network that connects the intestine, via the stomach, medullary reticular formation, and hypothalamus to craniofacial muscles. The network enables anorectic gut peptides to elicit food rejection.

One core concept associated with endogenous GLP-1 relates to its presumed role in regulating physiological satiety (Dailey and Moran, 2013). However, although ileal GLP-1 infusions produced potent appetite-suppressing effects, ileal GLP-1 receptor antagonism failed to augment food intake. This was also the case for each enteric and brain population engaged by ileal GLP-1: Although ablating these neurons rendered GLP-1 infusions completely ineffective, baseline eating patterns were strictly conserved. It is therefore

unlikely that endogenous GLP-1—at least the quantities released from non-absorptive segments of the lower intestine—functions to regulate physiological satiation. Instead, intestinal GLP-1 may protect against nutrient malabsorption (Dailey and Moran, 2013; Drucker, 2018; Schirra and Göke, 2005), consistent with a major role for non-absorbing distal gut segments in GLP-1 secretion (Panaro et al., 2020). In fact, we found that both ileal GLP-1R antagonism and intestinofugal neuron ablation abolished the ileal brake reflex, an ileal-gastric defensive mechanism triggered by nutrient malabsorption (Schirra and Göke, 2005). Consistent with the above, recent findings show that GLP-1 levels increase in response to the luminal release of inflammatory and bacterial signals, as well as after induction of intestinal ischemia (Lebrun et al., 2017). Now, although our principal aim was to study the neural transduction of GLP-1 released in the distal gut, future experiments involving infusions into the upper intestine may reveal a more specific role for proximal gut GLP-1 release (Panaro et al., 2020) in physiological satiety.

Although GLP-1 has traditionally been considered an incretin (Schmidt et al., 1985), its presumed endocrine actions have been challenged (Burcelin et al., 2009; D'Alessio, 2016; Vahl et al., 2007). It is therefore noticeable that we failed to observe changes in baseline blood glucose levels after ileal GLP-1 infusions. This is in contrast with the conspicuous inhibitory effects of these infusions on gastric motility and eating. Our data are therefore consistent with the notion that the insulinotropic effects of GLP-1 may derive from the peptide's antimotility properties (Nauck et al., 1997; Tong and D'Alessio, 2014). Indeed, the promotility drug erythromycin antagonizes the deceleration of gastric emptying by GLP-1, thereby unveiling its insulinotropic effects (Meier et al., 2005). Moreover, whereas proglucagon-derived gut peptides do regulate glucose levels, these effects may be motility-dependent since plasma insulin levels following glucose administration remain normal even in the absence of gut-derived GLP-1 (Song et al., 2019). Our data therefore reinforce the concept that islet GLP-1 may play an important role in regulating glucose homeostasis (Chambers et al., 2017). Future experiments combining tissue-specific manipulations of pancreatic preproglucagon (Chambers et al., 2017) with intestinal infusions may assist in uncovering the logic underlying GLP-1's insulinotropic effects.

In our experiments, paresis-induced stomach distension emerged as an obligatory mechanism linking ileal GLP-1 to appetite suppression. Thus, ileal GLP-1 effects were eliminated upon either ablating inhibitory nitric oxide gastric neurons or chemically activating excitatory cholinergic gastric neurons. Conversely, ileal GLP-1 effects were mimicked by either chemically activating nitric oxide, or ablating cholinergic, gastric neurons. Our data thus show that enteric gastric neurons are essential controllers of appetite (Robinson et al., 1988). Since previous findings demonstrated a role for nitric oxide in facilitating GLP-1 effects (Grasset et al., 2017; Rotondo et al., 2011), we propose that this mechanism is mediated by a defined subpopulation of Nos1 gastric neurons. Specifically, ileal GLP-1 caused anorexia and stomach distension via intestinofugal-mediated sympathetic reflexes (Furness, 2006; Hibberd et al., 2020) that activate gastric nitric oxide neurons. Interestingly, we also found that GLP-1-induced distension signals were conveyed to the brain via spinal (Spencer et al., 2016), not vagal (Berthoud et al., 2004), gastric sensory innervation. This is consistent with the notion that vagal afferents may be relevant for systemic (Borgmann et al., 2021), but not for gut or portal (Rüttimann et al.,

2009), GLP-1 sensing. In addition, we uncovered a non-canonical innervation of nitric oxide gastric neurons by sensory ganglia, suggesting that in addition to stretch sensors (Robinson et al., 1988), the gut may communicate the motility state of its musculature to the brain via synaptic signaling. Overall, the data point to a dissociation between vagal versus spinal gut-brain pathways that primarily detect rewarding (Han et al., 2018) versus malabsorption signals, respectively.

Such dissociation between vagal versus spinal systems is unanticipated. As is the case for nutrient sensing, perception of gut tension has historically been attributed to afferent endings of the vagus nerve (Berthoud and Powley, 1992; Blackshaw et al., 2007; Cannon and Washburn, 1993; Umans and Liberles, 2018). Thus, whereas vagal tension receptors have been suggested to detect stimuli such as distension and contraction of the gut wall, serosal afferents would respond to gut wall elongation (Berthoud et al., 2004; Blackshaw et al., 2007). In contrast, spinal gut afferents have been generally relegated to mediating high-threshold, painful sensations (Blackshaw et al., 2007). In line with the current consensus, an intense interest in vagal gut innervation has recently emerged (Bai et al., 2019; Kim et al., 2020; Williams et al., 2016). Yet, a closer examination of gut sensory innervation indicates that vagal nodose ganglia are unlikely to be the sole transducers of gut wall distension. In fact, intestinal segments scantily innervated by the vagus, e.g., the distal colon and rectum, generate graded sensations ranging from fullness to discomfort (Corsetti et al., 2004; Lynn et al., 2003)—just like the sensations evoked by the vagally innervated stomach. Similar conclusions may be reached from examining other internal organs. For example, the sensation of bladder fullness, a percept comparable to the sensation of stomach distension (Iggo, 1955; Merrill et al., 2016), is independent of vagal afferent signaling (since the bladder is deprived of vagal terminals; Keast and De Groat, 1992; Umans and Liberles, 2018). Finally, other well-studied mechanical sensations, such as light and sensual touch, are known to reach brain centers via spinal, not vagal, pathways (Craig, 2002). Thus, spinal sensory neurons are likely major contributors to gastric interoception.

None of the above is meant to imply that vagal afferents fail to play key roles in signaling ileal GLP-1. Consistent with our analyses at baseline states, GLP-1R ablation in Wnt1+ neurons (Wnt1 is an enteric neuron marker; Brokhman et al., 2019) failed to affect appetite or gut motility (Varin et al., 2019). However, GLP-1R ablation in Phox2b+ neurons significantly accelerated gastric emptying (Varin et al., 2019). Thus, although the primary function of GLP-1R signaling in ileal enteric neurons may be to trigger the ileal brake reflex, it is plausible that ileum-innervating GLP-1R+ vagal afferents regulate standard feeding (Brierley et al., 2021). Future studies may explore the physiological function of ileal GLP1R+ sensory fibers by combining site-specific vagal denervation with local GLP-1 infusions.

Finally, we note that different nodes of this novel network may be targeted to ameliorate the appetite loss, belching, and bloating typical of gastroparesis (Camilleri et al., 2018). In this regard, we stress that intestinal GLP-1 effects were independent of GLP-1R expression in the *area postrema*, a circumventricular area implicated in nausea induced by GLP-1 analogs (Kanoski et al., 2016; Zhang et al., 2021). We conclude that, unlike the case of GLP-1 analog-induced sickness, targeting gut neurons may be essential to halt the anorexia and

abdominal bloating associated with gastric paresis. Thus, of therapeutical interest would be employing peripheral neuromodulation approaches to target intestinofugal and gastric neurons for inter-organ control of interoceptive states.

Limitations of the study

Of note, our intravital imaging approach to enteric neurons made use of lightly anesthetized mice. Different, and certainly more accurate, effects would be obtained if we had used awake animals. Likewise, we have not monitored L cell activity or ileal GLP-1 release in real time. As peripheral neurobiology techniques continue to improve, an important long-term goal is to develop intravital imaging approaches to monitor enteroendocrine and myenteric neurons in behaving animals, especially during feeding.

STAR★METHODS

RESOURCE AVAILABILITY

Lead contact—Further information and requests for reagents should be directed to and will be fulfilled by the Technical Contact Wenfei Han (wenfei.han@mssm.edu).

Materials availability—This study did not generate new unique reagents.

Data and code availability

- Behavioral, electrophysiological, anatomy, and analyzed intravital imaging data have been deposited at Mendeley Data and are publicly available as of the date of publication. DOIs are listed in the key resources table.

- This paper does not report original code.

- Any additional information required to reanalyze the data reported in this paper is available from the technical contact upon request.

EXPERIMENTAL MODEL AND SUBJECT DETAILS

All experiments presented in this study were conducted according to the animal research guidelines from NIH and were approved by the Institutional Animal Care and Use Committee of Icahn School of Medicine at Mount Sinai.

Experimental animals—A total of 541 adult male mice were used. Strain details and number of animals are as follows:

221 C57BL/6J (Jax Mouse Strain #000664)

61 Glp1r-ires-Cre (Jax Mouse Strain #029283)

5 Gcg^{iCre} × Ai32 (Jax Mouse Strain #030663 and #024109)

5 Ai32 (Jax Mouse Strain #024109)

5 Gcg^{iCre} (Jax Mouse Strain #030663)

5 Gcg^{iCre} × CAG-LSL-Gq-DREADD (Jax Mouse Strain #030663 and #026220)

2 Glp1r-ires-Cre x Ai148D (Jax Mouse Strain #029283 and #030328)

5 B6J.ChAT-IRES-Cre x Ai148D (Jax Mouse Strain #031661 and #030328)

22 Vglut2-ires-Cre (Jax Mouse Strain #016963)

1 Vglut1-ires2-Cre (Jax Mouse Strain #023527)

90 B6-iDTR (Jax Mouse Strain #007900)

51 B6J.ChAT-IRES-Cre (Jax Mouse Strain #031661)

52 Nos1^{cre} (Jax Mouse Strain #017526)

1 Ai9 (Jax Mouse Strain #007914)

3 Ai9 × B6J.ChAT-IRES-Cre (Jax Mouse Strain #007914 and #031661)

2 Ai9 × Nos1^{cre} (Jax Mouse Strain #007914 and #017526)

1 Ai9 × Glp1r-ires-Cre (Jax Mouse Strain #007914 and #029283)

9 CAG-Sun1/sfGFP (Jax Mouse Strain # 021039)

All mice used in behavioral experiments were individually housed under a 12hr. light/dark cycle. At the time of the behavioral experiments, animals were 12–20 weeks old and weighted approximately 25–28 grams. All animals were used in scientific experiments for the first time. This includes no previous exposure to pharmacological substances or alternative diets. Health status was normal for all animals. Animals used for anatomical tracing studies were group housed and 3 weeks old at the time of injection.

METHOD DETAILS

The following provides details on viral and drug injections, catheterizations, denervation, myogram electrode implantation, and optical fiber/high-density probe implantation for each mouse strain (see also Table S2). All surgeries were performed in a Biosafety Level 2-approved laboratory. In all cases, preoperative analgesia: 0.05 mg/Kg Buprenorphine (*s.c.*); anesthesia induced by 3% and maintained by 1.5% ~2% Isoflurane; postoperative analgesia: 0.05 mg/Kg Buprenorphine (s.c.) per day for three consecutive days. The surgical areas were shaved and cleaned with iodine soap and wiped with 70% isopropyl alcohol. All incisions were thoroughly disinfected with a layer of Baytril ointment. All surgeries were performed under stereomicroscopes, with animals placed on a heated pad (CMA 450; Harvard Apparatus, Holliston, MA). After surgery, animals were allowed to recover under infrared heat until they chose to reside in the unheated side of the cage.

Stomach or ileum injections—Three week-old mice received one of rAAV2-retro.hSyn.Cre, rAAV2-retro-hSyn-EGFP, AAV-DJ-hSyn-DIO-rM3D(Gs)-mCherry, AAVDJ-hSyn-DIO-rM3D(Gi)-mCherry, AAV-DJ-hSyn-DIO-EGFP, AAV1-flex-taCasp3,

Mouse IgG-SAP, Anti-DβH-sap, or H129 CMV-EGFP. Animals injected with H129 CAG-LSL-TK-tdTomato were 4-weeks-old, which was one week after they received a viral injection (rAAV2-retro.hSyn.Cre) in celiac ganglion (see below for details on celiac injections). The abdomen of the animal was shaved and cleaned. A midline incision was made into the abdomen. The stomach or ileum (about 5 cm proximal to ileocaecal valve) were exteriorized through the midline incision. The viral constructs or chemicals were loaded into a Nanofil™ 36G beveled needle (WPI, Sarasota, FL) and Silflex™ tubing (WPI, Sarasota, FL), connected to a Nanofil™ 10μl syringe (WPI, Sarasota, FL) and mounted on a Pump 11 Elite Nanomite (Harvard Apparatus, Holliston, MA). Multiple 30nL injections were made at 10nL/s into each submucosal puncture. The needle tip was carefully manipulated to avoid mesenteric blood vessels. After completing the infusions, needle was left in place for 5s before extraction to ensure full absorption. Each animal received a total volume of 1μL. Sterile suture was then applied to the skin.

Nodose ganglia injections—Mice injected with unconjugated saporin (Blank-SAP) or cholecystokinin-conjugated saporin (CCK-SAP) were 3 weeks old. Animals injected with AAV5-Ef1a-DIO EYFP, H129 CAG-LSL-TK-tdTomato, or diphtheria toxin were 4-weeks-old, which was one week after they received a gastric viral injection (rAAV2-retro.hSyn.Cre or rAAV2-retro-hSyn-EGFP) as described above. Nodose ganglia injections were performed as described previously (Han and de Araujo, 2021). Briefly, a ventral midline incision was made along the length of the neck; submandibular glands were retracted along with sternohyoid and omohyoid muscles to expose the trachea and carotid artery. The vagus nerve was separated from the carotid artery with a Spinal Cord Hook (FST, Foster City, CA) until the nodose ganglion became accessible. Viral or chemical aliquots were loaded into a Nanofil™ 36G beveled needle (WPI, Sarasota, FL) and Silflex™ tubing (WPI, Sarasota, FL). For each nodose ganglion, a total of 500nL volume of virus was delivered at 50nL/min using a Nanofil™ 10μl syringe (WPI, Sarasota, FL) mounted on a Pump 11 Elite Nanomite (Harvard Apparatus, Holliston, MA). Sterile suture was then applied to the skin.

Celiac ganglia injections—Animals injected with either rAAV2-retro.hSyn.Cre or rAAV2-retro-hSyn-EGFP were 3-weeks-old. Animals injected with one of AAV-DJ-hSyn-DIO-rM3D(Gs)-mCherry, AAV-DJ-hSyn-DIO-EGFP, AAV1-flex-taCasp3, AAV1-synP-FLEX-splitTVA-EGFP-B19G, EnvA G-Deleted Rabies-mCherry, or H129 CAG-LSL-TK-tdTomato, were 4-weeks-old, which was one week after they received a gastric viral injection (rAAV2-retro.hSyn.Cre) as described above. The abdomen of the animal was shaved and cleaned. A midline incision was made into the abdomen. The stomach was exteriorized through the midline incision. The stomach fundus was pulled towards the liver to expose the left and right celiac ganglia. Viral aliquots were loaded into a Silflex™ tubing (WPI, Sarasota, FL) connected with a Nanofil™ 36G beveled needle (WPI, Sarasota, FL). The needle tip was gently inserted into the ganglion, which was supported in place with a cotton tip. For each celiac ganglion, a total of 500nL volume of virus was delivered at 50nL/min using a Nanofil™ 10μl syringe (WPI, Sarasota, FL) mounted on a Pump 11 Elite Nanomite (Harvard Apparatus, Holliston, MA). Sterile suture was then applied to the skin.

Dorsal root ganglia injections—Animals injected with H129 CAG-LSL-TK-tdTomato were 4-weeks-old, which was one week after they received a gastric viral injection (rAAV2-retro.hSyn.Cre) as described above.

The back skin was shaved and cleaned. A midline incision was made with a scalpel. The skin was retracted aside. The trapezius, rhomboid and latissimus muscles were separated from the spinal cord with a periosteal elevator (GerVetUSA, Albertson, NY). The vertebrae at thoracic levels T8 through T10 were exposed using a Mini-Goldstein Retractors (FST, Foster City, CA). The vertebrae were secured with a Mouse Spinal Adaptor and Transverse Clamp (Stoelting, Wood Dale, IL). The lamina and pedicle were gently grinded with a micro drill (WPI, Sarasota, FL). Once DRGs were exposed and visualized, viral aliquots (H129 CAG-LSL-TK-tdTomato) were delivered using a NanofilTM 36G beveled needle connected to Silflex™ tubing (WPI, Sarasota, FL). For each DRG, a total of 500nL volume of virus was delivered at 50nL/min using a Nanofil™ 10μl syringe (WPI, Sarasota, FL) mounted on a Pump 11 Elite Nanomite (Harvard Apparatus, Holliston, MA). Sterile suture was then applied to muscle and skin.

Intrathecal infusions—Animals at the time of intrathecal injection were 4-week-old, which was one week after they received a gastric viral injection (rAAV2-retro.hSyn.Cre) as described above. The back skin was shaved and cleaned. A midline incision was made with a scalpel. After retracting the skin aside, the lumbar vertebrae were exposed. A NanofilTM 36G beveled needle connected to Silflex™ tubing (WPI, Sarasota, FL) was carefully inserted into the groove between the L5 and L6 vertebrae. A total of 5μl volume of Diphtheria Toxin was delivered at 1μL/min using a Nanofil™ 100μl syringe (WPI, Sarasota, FL) mounted on a Pump 11 Elite Nanomite (Harvard Apparatus, Holliston, MA). Sterile suture was then applied to skin.

Celiactomy—Animals at the time of intrathecal injection were 3-week-old. The abdomen was shaved and cleaned. A midline incision was made into the abdomen. The stomach was exteriorized through the midline incision. The stomach fundus was pulled towards the liver to expose the celiac ganglion. The celiac ganglion was carefully separated away from the celiac artery with a miniature forceps (FST, Foster City, CA). The base of the celiac ganglion was ligated before resection. Sterile suture was then applied to skin.

Subdiaphragmatic vagotomy—Animals at the time of subdiaphragmatic vagotomy were 3-week-old. The abdomen was shaved and cleaned. A midline incision was made into the abdomen. The liver and stomach were retracted aside to expose the esophagus. The branches of the vagus nerves innervating the stomach were carefully separated from both the esophagus and the left gastric artery and were bilaterally severed with an electrical cauterizer. A viral aliquot of H129 CMV-EGFP was then injected as described above. Sterile suture was then applied to muscle and skin.

Ileal-stomach connectivity* via *abdominal sympathetic ganglia—To demonstrate the existence of an ileal-sympathetic-gastric circuitry, we injected the retrograde, *Cre*-expressing virus AAV2-retro-hSyn.HI.EGFP-Cre virus into the muscle layers of the stomach, concomitant to injections into CG of the *Cre*-inducible construct AAV1-synP-

FLEX-splitTVA-EGFP-B19G, which expresses the rabies virus replication G factor. Three weeks later, we injected the *Cre*-dependent, G factor-deficient monosynaptic rabies virus EnvA- G-Rabies-mCherry into CG. This, by definition, specifically mapped inputs to CG^Stom. To ablate CG^Stom noradrenergic (sympathetic) neurons ("CG^NA–Stom") *in vivo,* we targeted the stomach with the immunotoxin anti-DβH-saporin, a compound that acts to specifically ablate noradrenaline cells via retrograde uptake (Milstein etal., 2007). For activating CG^Stom neurons using chemogenetics, we injected the construct AAV2-retro-hSyn.HI.EGFP-Cre into the stomach, followed by injections of the *Cre*-dependent excitatory construct AAV-DJ-hSyn-DIO-rM3D(Gs)-mCherry into CG^Stom (while sparing the superior mesenteric ganglion).

Sham-feeding gastric fistulae—Animals at the time of gastric fistulae surgeries were 8-week-old. The abdomen was shaved and cleaned. A midline incision was made into the abdomen. The stomach was exteriorized through the midline incision and a purse string suture was placed in the fundus. A Female Luer (1/4" ID, Cole-Parmer, Vernon Hills, IL) was inserted and closed by the purse string suture. The rectus abdominis and abdomen skin were closed and sutured across the luer. The matching Male Luer Lock (Cole-Parmer, Vernon Hills, IL) was rotated and tightened to the luer end.

Intragastric balloon—Animals at the time of gastric balloon implantation were 8-week-old. The abdomen and dorsal back skin of the animal were shaved and cleaned. A midline incision was made into the abdomen. The stomach was exteriorized through the midline incision and a purse string suture was placed in the fundus. The collar of a mouse jugular vein catheter (1 to 3Fr, fit 22 Ga, Instech laboratories, Plymouth Meeting, PA) was sealed to a latex balloon (Size 4,0.06ML, Harvard Apparatus, Holliston, MA). The balloon was then inserted into the stomach lumen. The purse string was tightened around the tubing, which was then tunneled subcutaneously to the dorsum via a small hole made into the abdominal muscle. A small incision to the dorsum between the shoulder plates was then made to allow for catheter exteriorization. Sterile suture was then applied to the abdominal incisions.

Gastric electromyogram probe implant—Animals at the time of gastric electromyogram probe implant were 8-week-old. Two twisted Formvar-Insulated Nichrome Wires (Diameter: Bare 0.002 inch. A-M system) were covered with polyethylene tubing (PE20, 0.15" x 0.45", Braintree scientific). The tips of the nichrome wires were bared and exposed. One bare wire tip was soldered to a Male Miniature Pin Connector (520200, A-M Systems). The other bare wire tip was inserted through a 30G needle, and the tip bent and used for the implants into the stomach. For implants, preoperative analgesia consisted of 5mg/Kg Carprofen, anesthetic was 2% Isoflurane throughout and postoperative analgesia, 30mg/Kg Ibuprofen. The skin of the upper abdomen was shaved and open to expose the underlying musculature. The needle was then used for insertion of the wire into the stomach via a small hole made into the abdominal muscle, with the bare wire hooked into the stomach. A suture was used to fix the wire in place. To verify the efficacy of the recordings, at the end of each session animals were administered the gut motility-inducing drug metroclopramide hydrochloride (10mg/kg i.p.). Recordings were performed using the electromyogram module of a multichannel acquisition processor (Tucker-Davis

Technologies, 3052Hz sampling rate). The male pin connector was attached to the female connector, which had been soldered to a recording headstage. Laser pulses timestamps were synchronized to the recordings via external TTL pulses into the TDT system. The dorsal neck skin was then closed with sterile suture.

Intra-ileum catheterization and infusions—Animals at the time of experiments were 8-week-old. The abdomen and dorsal back skin of the animal were shaved and cleaned. A small incision to the dorsal neck, and a midline incision into the abdomen, were made. The ileum was exteriorized through the midline incision. A purse string suture was placed on the ileal wall at 5cm proximal to ileocaecal valve, into which the tip of MicroRenathane tubing (0.025", Braintree Scientific, Braintree, MA) was inserted. The purse string was tightened around the tubing, which was then tunneled subcutaneously to the dorsum via a small hole made into the abdominal muscle. A small incision to the dorsum between the shoulder plates was then made to allow for catheter exteriorization. The abdominal incision was then closed with sterile suture. All infusates (CCK-8 10ng/Kg, GLP-1 10,50,100nMol/Kg, Exendin-4 10ng/kg, 20% Intralipid [0.5% body weight]), bile salts (5mg/mice, 0.5% body weight) were freshly prepared with sterile saline and 0.1mL infused at 0.1mL/minute.

Rationale for intra-ileal GLP-1 doses and preparation—Previous assessments of GLP-1 concentrations in the mouse gut estimate ileal concentrations at ~50pmol/g GLP-1 (e.g., Paternoster and Falasca, 2018). According to our measurements, the total mass of the ileum of a 30g mouse is approximately 0.1g. Thus, approximately, each animal has ~16.5ng of ileal GLP-1. Assuming ~10–15% of released GLP-1 reaches circulation (Holst, 2007), we decided to infuse ~12% of the estimated total concentration (i.e., 2ng/30g mouse or 20pMol/Kg). In a 30g mouse, this corresponds to 25×10^{-4} of a GLP-1 dose that is effective intra-peritoneally (e.g., Jessen et al., 2012). Our initial tests indeed showed that this dose, when injected into the mouse ileal lumen, induces significant decreases in gastric contractions as well as gastric distension. We also produced a dose-response analysis which is shown in Figure S1I. Based on the above verifications, we applied 20pMol/Kg for all short-term tests (*in vivo* electrophysiology and intravital ileal confocal microscopy) and 50pMol/Kg (25pMol/Kg twice per hour) for longer-term food intake tests, thereby minimizing dipeptidyl-peptidase-4 cleavage.

We thus stress that the dose selected conservatively approximates increases in serum concentrations of GLP-1 observed in humans following a meal (Vilsboll etal., 2001), or following duodenal infusion of lipids (Layer etal., 1995). In these studies, resting plasma concentrations of GLP-1 were between 10–20 pMol/liter, and increased to a peak of 30–60pMol/liter within 60 minutes of meal feeding or lipid infusion. In mice, a slightly smaller magnitude increase in plasma GLP-1 is observed following oral administration of glucose: an increment of ~15pMol/liter (Windelov et al., 2017). We made the conservative assumption that systemic GLP-1 signaling may occur despite mechanisms of rapid degradation, i.e., we do not exclude the possibility of minimal degradation between infusion and the initiation of physiological signaling. Thus, our studies demonstrating the sufficiency of ileal GLP-1R+ enteric neurons in mediating intestinal GLP-1 effects were conservatively designed as they do not exclude the possibility that GLP-1 may act extra-intestinally.

Intra-oral catheterization and infusions—Animals at the time of were 8-week-old. The face of the animal was shaved and cleaned. A small incision at the dorsal back skin and a small incision into the oral mucosa, at the junction between the inframargin of the masseterand the supramargin of the mandible, was made. A MicroRenathane tubing (0.025", Braintree Scientific, Braintree, MA) was inserted into the oral cavity with a purse string tightened around. The tubing was then tunneled subcutaneously to the dorsum and exteriorized.

Intravital ileal window for confocal microscopy—For intravital confocal imaging of calcium transients in gastric and ileal neurons, we generated Glp1r-ires-CrexAi148D (Cre-dependent GCaMP6f), B6J.ChAT-ires-CrexAi148D, or injected the Cre-inducible construct AAV1-syn-FLEX-jGCaMP8m into the stomach corpus of 3-week-old Nos1^{cre} animals. These injections were needed as it appeared that Nos1^{cre}xAi148D were not viable. When 6-week-old, the animals received the ileal catheterization as above, followed by a gastric or ileal window placement for intravital confocal microscopy, as previously described (Rakhilin et al., 2019). Briefly, a round cover slip (ø15 mm, Electron Microscopy Sciences, Hatfield, PA) was glued (Ultra Gel Control, Loctite, Hartford, CT) between a 12×24×1.5 mm stainless steel fender washer and a custom 13×14×1.5 mm polypropylene ring. A purse string suture was placed on the incision edge between the Rectus abdominis and the abdominal skin. The distal ileum (3 cm distal to the ileocaecal valve) or stomach were exteriorized through the midline incision and gently folded and placed to maximize the field of view through the cover glass. Drops of Low Toxicity Silicone Adhesive (KWIK-SIL, WPI, Sarasota, FL) were carefully applied to the outer surface of the distal ileum before being attached to the cover glass. Then, the ileum was gently pushed back into the abdominal cavity. The purse string suture was tightened to the groove of the customized titanium ring. Animals were under continuous 1.5% Isoflurane anesthesia. Calcium imaging was performed using a LeicaSP8 confocal microscope with a 10× objective lens. Upon visualizing GCaMP6f or jGCaMP8m-expressing neurons, continuous imaging series were acquired at 4 frames/sec with FOV=2.25mm^2. After a corresponding 10 minutes-long baseline period, 0.1mL of 20nMol/Kg GLP-1 was infused via the ileal catheter at 0.1mL/min, after which a 20 minutes-long post-GLP-1 image series was recorded.

Ileal intravital optogenetic stimulation and ileal GLP-1 content—Gcg-ires-Cre×Ai32 and Ai32 animals were implanted with abdominal glass windows over the ileal region. Under continuous 1.5% Isoflurane anesthesia, animals were mounted over a horizontally rotating (30 rpm) platform. A 70mW 480nm laser was placed 3mm away from the intravital ileal window, and activated at 1Hz. One hour after the stimulation, the intravital window has quickly detached. Distal ileum and connected mesenteric membrane were ligated, dissected and weighed before immediately placed into liquid nitrogen. Animals were later transcardially perfused for anatomy analysis. Unfrozen ileum tissue was dissected by scissor and abrader. For assessing depletion of GLP-1 from L-Cells after laser stimulation: Centrifuged supernatant extracts containing GLP-1 were measured using an ELISA kit (Abcam, ab229413, Human GLP-1 (7–36) CatchPoint SimpleStep ELISA® Kit). The signals were recorded by a Molecular Devices' plate reader (SpectraMax M3) supported by SoftMaxPro software. The excitation value was set as530nm; the emission value was set

as 590 nm; and the cutoff value was set as 570 nm. The tissue GLP-1 concentration was determined by analyzing the standard curve.

PseudoRabies virus (PRV) injections—Animals at the time of injections were 8-week-old. A small incision was made on the cheek to expose either masseter muscle or the parotid gland. A small incision was made to the submandibula to expose the digastric muscle. Viral aliquots (PRV-CMV-EGFP Ba-152) were delivered to either the masseter, digastric, glossal, or parotid gland with a NanofilTM 36G beveled needle connected to SilflexTM tubing (WPI, Sarasota, FL). For each target, a total of 200nL volume of virus was delivered at 50nL/min using a NanofilTM 10µl syringe (WPI, Sarasota, FL) mounted on a Pump 11 Elite Nanomite (Harvard Apparatus, Holliston, MA). The skin was then closed with sterile suture.

Intracerebroventricular injections—Animals at the time of were 8-week-old. Cannulae for intracerebroventricular infusions were obtained from Plastics One (Roanoke, VA). GLP-1 (2µg/mL) was freshly prepared in aCSF (used as vehicle control) and infused into the 4th ventricle over the *Area Postrema* at AP =7.5 mm, ML = ±0 mm DV = −4.5 mm, total of 1µL (2ng GLP-1), at 0.1µL/min. Infusions took place 5 minutes before the 1h-long food intake tests.

Stereotaxic viral injections and optical fiber implantation—Animals at the time of surgery were 8-week-old. Injections were performed with a Hamilton 1.0µL Neuros Model 7001KH syringe, at a rate of 20nL/min. In what follows, and for each mouse strain, we first list the viral construct injected, then the relevant stereotaxic coordinates for the injections are described. When applicable, the optical fibers were implanted 0.3 mm above the viral injection coordinate immediately after the infusion was accomplished bilaterally. Optical fibers were obtained from Doric Lenses, Canada. Stereotaxic coordinates are with respect to *bregma,* according to a standardized atlas of the mouse brain (Keith Franklin & George Paxinos, *The Mouse Brain in Stereotaxic Coordinates,* Compact 3rd Edition, Academic Press, 2008).

Mouse strain **Vglut2-ires-Cre**

Injection Location PSTn

Viral construct AAV1 hSyn FLEx mGFP-2A-Synaptophysin-mRuby (300nL unilateral)

AAV5-EF1a-double floxed-hChR2(H134R)-EYFP / AAV1/AAV5-Ef1a-DIO EYFP (300nL each, bilateral)

AAV1-flex-taCasp3 / AAV-DJ-hSyn-DIO-EGFP (300nLeach, bilateral)

PRV CAG-DIO-TK–GFP (Ba-2017, 100nL unilateral)

Coordinates: AP:−2.4mm, ML: ±1.1mm, DV −4.95mm.

PCRt optic fiber implant:

Coordinates: AP:−5.2mm, ML: ±1.4mm, DV −4.0mm.

Mouse strain **Glp1r-ires-Cre**

Injection Location *AP*

Viral construct AAV1-flex-taCasp3 / AAV-DJ-hSyn-DIO-EGFP (500nL)

Coordinates: AP:−7.5mm, ML: ±0mm, DV −4.5mm.

Mouse strain **Vglut1-ires-Cre**

Injection Location lateral reticular nucleus, LRN

Viral construct AAV1-synP-FLEX-splitTVA-EGFP-B19G (300nL unilateral) and 7 days later, EnvA G-Deleted Rabies-mCherry (300nL unilateral).

Coordinates: AP:−7.6mm, ML: ±1.7mm, DV −6.5mm.

Intestinofugal neuron (IFN) gene expression analysis—Three-week-old CAG-Sun1/sfGFP mice received an intra-celiac viral injection as described above (rAAV2-retro.hSyn.Cre). Two weeks later, the mice were perfused with heparin (10mU/L) saline. The ileum was dissected out and thoroughly rinsed after separation of the mesentery tissue and removal of luminal contents. The ileum was gently rubbed in an ice-cold dissection solution (ice-cold DMEM:F12 (1:1) supplemented with 1% pen/strep and 12.5 mM d-glucose) in order to remove most of the mucosa. The intact myenteric tissue was then disaggregated and sliced with fine tip scissors in an ice-cold nuclear extraction buffer containing 73mM NaCl (Thermo Fisher Scientific, catalog no. AM9759), 5mM Tris-HCl pH 7.5 (Thermo Fisher Scientific, catalog no. 15567027), 0.5mM CaCl2 (VWR, catalog no. 97062–820), 10.5mM MgCl2 (Sigma-Aldrich, catalog no. M1028), and 0.5% CHAPS (Millipore) for 10 minutes. Large debris were removed with a 40μm strainer (Falcon). The homogenate was spun at 1000g for 8 min at 4°C, the precipitate washed once and resuspended in 500ml 1% PBS-diluted BSA. Dissociated nuclei were then treated with Hoechst 33342 (Invitrogen, 1:1000) and anti-NeuN-Alexa Fluor 647 antibody (Abcam, 1:500, ab190565, clone EPR12763) for 15 min on ice. Stained nuclei were then washed and resuspended in 1% PBS-diluted BSA for FACS sorting using a Miltenyi Tyto microfluidic sorter (Miltenyi Biotec). The IFN nuclei (Hoechst$^+$ NeuN$^+$ GFP$^+$) and the non-IFN enteric neuronal nuclei (Hoechst$^+$ NeuN$^+$ GFP$^-$) were separated into different 1.5 ml EP tubes. 5μL of isolated nuclei were assessed under a fluorescent microscope (Nikon) for GFP positive enrichment. The total RNA from the sorted enteric nuclei were extracted using the RNeasy Plus Micro Kit (Qiagen). The RNA reverse transcription and the real-time PCR were performed by Quintara Biosciences Co. (Boston, USA). The real-time PCR primers used for GLP1R gene were designed as follows:

1. GLP1R-Forward: CGGAGTGTGAAGAGTCTAAGCG

2. GLP1R-Reverse: ATGGCTGAAGCGATGACCAAGG.

The real-time PCR primers used for Actb gene were designed as follows:

1. Actb-Forward: CATTGCTGACAGGATGCAGAAGG;

2. Actb-Reverse: TGCTGGAAGGTGGACAGTGAGG.

Histological procedures including Herpes Simplex Virus labeling—Mice were deeply anesthetized with a ketamine/xylazine mix (400 mg ketamine + 20 mg xylazine kg body weight^{-1} I.P.). All animals were perfused with filtered saline, followed by 4% paraformaldehyde. Following perfusion, brains were placed in 4% paraformaldehyde for 24 hours and then moved to a 20% sucrose solution in 0.02 M potassium phosphatebuffer (KPBS, pH 7.4) for 2 days. Brains were then frozen and cut into four series 40μm sections with a sliding microtome equipped with a freezing stage. To identify fiber and electrode locations, relevant sections were identified and mounted on slides. Sections were then photographed under bright field and fluorescence. For *Herpes Simplex* Viruses visualization, 3 or 4 or 5 days after viral injection, mice were perfused, and brains cut at 40μm. The mCherry signal was amplified with Rabbit-anti-mCherry (Abcam, ab167453,1:500) followed by TRITC-conjugated affinipure Goat anti-Rabbit (IgG (H+L) 111–025-144, Jackson Immuno, 1:200). The EYFP signal was amplified with Goat anti-GFP antibody (FITC), (ab6662, Abcam, 1:500) followed by Alexa Fluor® 594 AffiniPure Goat Anti-Rabbit (IgG (H+L), 111–585-103, Jackson Immuno, 1:200).

c-Fos immunoreactivity—Fos immunoreactivity was used to determine the effects of chemogenetic, intra-ileal infusions, and intra-gastric balloons, on neuronal activity. Ninety minutes after the appropriate stimulation, mice were sacrificed and perfused as described above. To visualize Fos immunoreactivity, either the ABC/DAB procedure or immunofluorescence was used. Briefly, brain sections were incubated with Rabbit Anti-c-Fos antibody (Rabbit Anti-c-Fos ab190289,1:1000), followed with Biotinylated Goat Anti-Rabbit IgG Antibody (BA-1000, Vector Laboratories, 1:500), then reacted with avidin-biotin-peroxidase complex ("ABC" method, Vectastain Elite ABC kit, Vector Laboratories, 1:200). A nickel diaminobenzidine (Nickel-DAB) glucose oxidase reaction was used to visualize Fos-like immunoreactive cells. To visualize Fos via immunofluorescence, slices were incubated with Rabbit Anti-c-Fos antibody (Rabbit Anti-c-Fos ab190289, 1:1000), followed by FITC-conjugated affinipure goat anti-rabbit (IgG (H+L) 111–095-144, Jackson Immuno, 1:200). Fos expression was analyzed and quantified as follows: Coronal sections at ~160μm intervals were photographed at 10× magnification and montaged with ImageJ to preserve anatomical landmarks. Fos+ neurons in each section were detected and counted using ImageJ and expressed as the cumulative sum of Fos+ neurons within the relevant regions for each animal.

Gut and celiac ganglia whole-mount immunostaining and tissue clearing—Whole tissue clearing as described previously (Renier et al., 2014). Briefly, animals were anesthetized and perfused with saline and 1%PFA. The celiac ganglia or gut tissue were dissected, opened, and cleaned in a 1%PFA solution. Attached connective tissues were removed, and for gut the tissue was flattened on a glass plate. After 24h fixation with 4% PFA at 4°C, tissues were washed with PBS for 1hr x 3 times. Tissues were then dehydrated at room temperature in a series of methanol/B1n solutions (20%, 40%,60%,80%,100%,100%), 30 min for each concentration. After delipidation

(DiChloroMethane, overnight) and discoloration (10% H_2O_2/methanol, overnight) at 4°C, tissues were rehydrated at room temperature in a series of methanol/B1n solutions (80%, 60%, 40%, 20%, 0%, 0%), 30 min for each concentration. Tissues were transferred into a PTxwH solution with 1:1000 primary antibody and vibrated in an incubator at 37° C for 72hs. After thoroughly washed with PTxwH solution for48hs, tissues were shaken in 1:500 secondary antibody PTxwH solution for 72hs and then washed out for 48hs. Each tissue was next imbedded with a mixture of dichloromethane (Sigma)/methanol (2 volumes/1 volume) for 3hr, and then with 100% dichloromethane for 15 min, twice. The tissue was then transferred to a cover-glass bottomed chamber and then finally cleared with 100% dibenzyl-ether (Sigma) for 1hr twice and prepared for confocal imaging.

Confocal FRET—Förster (fluorescent) resonance energy transfer (FRET)-based confocal microscopy was employed to assess the diffusion of GLP-1 infused into ileum. FRET generates fluorescence signals sensitive to separation within the 1–10nm range (Jares-Erijman and Jovin, 2003). We infused the ileum with a synthetic GLP-1[7–36] containing a biotin label at the N-terminus. Cleavage by DPP-4 would thus separate the two biotin-conjugated amino acids from the C-extended remaining if the peptide. A monoclonal FTIC anti-Biotin antibody was used to detect N-terminal-conjugated biotin. To detect the C-extended portion of GLP1[7–36], a polyclonal Rabbit-anti-GLP1 antibody and a secondary Alexa Fluor 594-conjugated AffiniPure Donkey Anti-Rabbit IgG antibody. We therefore used the energy transfer principle of FRET to detect forms of the peptide in which the donor (N-terminal biotin) was separated from the C-terminally extended GLP-1[7–36] (acceptor) by less than 10nm (i.e., non-cleaved forms of GLP-1[7–36]). Images were acquired using a confocal Leica TCS SP8 STED 3X. FRET signals thus represent the distribution of full-length, un-cleaved biotin-conjugated GLP1[7–36]. Note that FRET signals do not include endogenous GLP-1 (since it is not conjugated to biotin). Within 15min of injections into ileum, mice were perfused, the ileum was isolated and prepared into 5μm frozen sections. The sections were then incubated with the GLP1[7–36] primary antibody, the Alexa594-conjugated secondary antibody, and the FITC anti-Biotin antibody. To assess FRET donor-only scattering, donor control sections were incubated only with the anti-Biotin-FITC antibody. To assess FRET acceptor-only scattering, acceptor control sections were incubated only with the GLP1 antibody and the Alexa594-conjugated secondary antibody. To compute FRET indexes, we employed the ImageJ *FRET and Colocalization Analyzer* plugin (1st version). FRET indexes represent the levels of energy transfer associated with changes in the donor-acceptor configurations. Detectable high values of FRET indexes were then interpreted as indexing the tissue distribution of intact forms of the biotin-conjugated GLP1[7–36] peptide.

Simultaneous single-neuron and electromyogram *in vivo* recordings with gastric balloon—Ten days before the recording session, a titanium headplate was secured to the skull with loctite 401 and dental cement, and a stainless-steel ground screw is implanted over the cerebellum. Muscles over the occipital bones are depressed, and a halo of dental cement is placed encircling a kwik-sil window over the occipital sutures, and Lambda is marked. Animals recovered for 3 days after implanting the headplate. Following recovery, animals were habituated to head restraint, for 3–5 days. Next, a twisted pair of

EMG wires was implanted into the greater curvature of stomach corpus, or near antrum, like the procedures described above. All EMG recordings were performed in awake, non-fasted animals. Briefly, 50μM formvar insulation nichrome wires (A-M systems) are striped of insulation over a 0.5mm length, a pair of these wires is aligned with a silicon stop glued about 1mm from the contact points, and the contact points are spaced about 1mm from each other. Wires are crimped to a 30G needle to facilitate quick placement during surgery. In the same procedure, the silicon balloon was implanted into the stomach. Two days after this surgery, the recording session was performed. Under isoflurane anesthesia, with buprenorphan analgesic, a craniotomy was performed, the dura matter carefully pierced with tungsten dissecting needles. To prevent the exposed brain from drying, mineral oil or FC-70 was layered over the craniotomy. To minimize drift, a custom fabricated steel holder is used to hold a silicon probe (Neuronexus). The PCB shaft of the probe was superglued to the holder, ensuring alignment of the axis of movement to the axis of the silicon shank. The probe holder was carried by a Sutter MP-285 manipulator, and slowly lowered (2–5μm/sec) through cerebellum or subthalamus to the recording region (respectively LRN or PSTn). The more anterior portion of LRN was targeted for recording, nominal coordinates relative to Lambda: AP 7.5 ML, ±1.5, DV 5.5–6. For PSTn, AP- 2.4, ML, ±1.1, DV −4.85. Electrophysiological landmarks were used to guide the recording depth. After lowering the recording probe, anesthesia was withdrawn, the probe allowed to stabilize for 10–15 minutes. Three to five trials of balloon inflation were performed, spaced 5 minutes apart. In each trial balloon volume is ramped from up to 700μL over a 40 second period, and then deflated at the same rate.

A custom-built integrated system was used to simultaneously acquire electromyogram, intraballoon pressure, single unit, and high-speed video records from head-fixed mice. Our system synchronizes the records to a master sample clock running at 24 kHz on a TDT RZ5 (Tucker-Davis Technology). Single unit activity of regions of interest were recorded with NeuroNexus 16 channel silicon probes, with the recording sites arranged in 4 sets of tetrodes. To reduce crosstalk from neck, masseter, and shoulder muscles, a common average is computed across all the recording sites, scaled, and then subtracted from each site. Whenever an exceptionally large single unit is present on all channels of a tetrode, this strategy is adjusted to compute sets of common averages, thereby preventing background subtraction artifacts. Discontinuous recordings are triggered by negative going peaks exceeding a threshold of 5.5 standard deviations of the background subtracted noise, digitized at 24 kHz. Units were sorted using OfflineSorter (Plexon). Differential EMG signals were measured using custom fabricated twisted pairs of 50-micron nichrome wire, with a design adapted from Keir Pearson, and miniaturized to reduce discomfort. EMGs were amplified and digitized on the RZ5 system at 8kHz. Video recordings were performed at 100 fps using a basler aca1300–60gm, with the IR cut filter removed. Hardware triggers were generated every 244th tick of the master sample clock of the TDT RZ5, ensuring that the video recordings can be aligned with the single unit and EMG data.

Slice electrophysiology—The coronal slices containing the hypothalamic parasubthalamic nucleus (PSTn) expressing AAV5-EF1a-double floxed-hChR2(H134R)-EYFP were prepared from VGlut2 mice. Briefly, mice were anesthetized with isoflurane

and then decapitated. Then brains were rapidly removed and immersed in cold (40°C) and oxygenated high-sucrose solution containing (mM): sucrose 220, KCl 2.5, NaH2PO4 1.23, NaHCO3 26, CaCl21, MgCl2 6 and glucose 10, pH 7.3 with NaOH). After being trimmed to a small tissue block containing the PBN, coronal slices (300 μm thick) were cut on a vibratome and maintained at room temperature (23–25 $^{\circ}$C) in a holding chamber with artificial cerebrospinal fluid (ACSF) (bubbled with 5% CO_2 and 95% O_2) containing (in mM): NaCl 124, KCl 3, $CaCl_2$ 2, $MgCl_2$ 2, NaH_2PO_4 1.23, $NaHCO_3$ 26, glucose 10, pH 7.4 with NaOH for recovery and storage. After recovery at room temperature for at least one hour, slices were transferred to a recording chamber constantly perfused with ACSF at a temperature of 33 $^{\circ}$C and a perfusion rate of 2 ml/min for electrophysiological experiments. Whole-cell patch clamp recording was performed in YFP-positive neurons in the parabrachial area under both voltage and current clamp. Micropipettes (3–4 MΩ) were made of borosilicate glass (WPI, Sarasota, FL) with a Sutter P-97 micropipette puller and back filled with a pipette solution containing (mM): K-gluconate 135, $MgCl_2$ 2, HEPES 10, EGTA 1.1, Mg-ATP 2.5, Na_2-GTP 0.3, and Na_2-phosphocreatin 10, pH 7.3 with KOH. Both input resistance and series resistance were monitored throughout the experiments and the former was partially compensated. Only recordings with stable series resistance and input resistance were accepted. To stimulate neurons with an optogenetic method, an LED-generated blue light pulses at different frequencies (5, 10 and 20 Hz) were applied to recorded neurons. All data were sampled at 3–10 kHz, filtered at 3 kHz and analyzed with an Apple Macintosh computer using Axograph X (AxoGraph).

Behavioral studies

Food restriction, intake, and Fos expression in intra-ileal infusion studies: In all studies involving intra-intestinal infusions, mice were single-caged, and food restricted, having access to 2.5g chow/day. This procedure allowed animals to maintain >90% of regular body weight. Experiments were performed daily, at the beginning of the dark cycle (7PM). One condition (i.e., one intestinal infusion followed by food intake) was performed on a given experimental day. Experiments were performed over consecutive days starting exactly at the same time (7PM). First, animals were placed under light isoflurane anesthesia and infused with saline or an experimental substance (one of GLP-1, Ex-4, cholic acid, CNO, Ex9–39,20%Intralipid). The volume infused was always 50μL over 10sec. Five minutes after the injections, animals were allowed *ad libitum* access to chow and, after 1hour, the remaining pellets were removed and weighted. For *Fos* studies, an identical procedure was adopted, but in this case no food intake was allowed after the injections, with animals perfused 90 minutes after the administration of the injections.

Behavioral apparatus for flavor conditioning: Behavioral experiments were conducted in either one of three identical mouse behavior chambers enclosed in a ventilated and sound-attenuating cubicle (Med Associates Inc., St. Albans, VT). Each chamber is equipped with two slots for sipper tubing placements, at symmetrical locations on one of the cage walls. All sippers are connected to a contact-based licking detection device allowing for measurements of licking responses with 10ms resolution. All lick timestamps were saved in a computer file for posterior analysis. Software controlled lasers and infusion pumps equipped with TTL input devices were connected to the behavioral chambers and

programmed to automatically trigger intra-intestinal infusions in response to the detection of licks. MED-PC IV (Med Associates) was used as the platform for programming all experiments.

Flavor conditioning: Mice were tested for learned avoidance to either intra-ileal GLP-1 orchemogenetic activation of celiac neurons. In each conditioning session, animals licked one of two different flavors available from one sipper. Flavors were blueberry or cherry flavors, 2g of Totally Light Drink Mix into 200mL of pre-prepared 1mM sucralose solution. For GLP-1 conditioning, each conditioning session was followed by either an intra-ileal/ventricular GLP-1 injection for one flavor or intra-ileal saline/intra-ventricular CSF for the other flavor. For celiac activation conditioning, each conditioning session was followed by either an intra-peritoneal injection of Clozapine-N-Oxide (1mg/kg, EnZo Life Sciences) for one flavor or intra-peritoneal saline for the other flavor. Conditioning sessions lasted for 1 hour and were performed for 4 consecutive days under food (16h) deprivation, alternating daily the flavor identities. Thus, there were 2 sessions associated with each specific flavor-stimulus pair. Flavor assignments were balanced across conditions and animals. To assess conditioned aversion, short-term (5 min) two-bottle preference tests between the two distinct flavors were performed before and following the conditioning sessions. These tests were performed in extinction. Short duration of this test aims to minimize postingestive influences. After conditioning, an identical test was performed to assess the formation of flavor preferences. The number of licks for each Flavor was recorded and used to calculate the preference ratio as follows:

$$\text{Preference ratio for } Flavor1 = \frac{n(Flavour1)}{n(Flavour1) + n(Flavour2)}$$

where n(Flavorx) denotes the detected number of licks to Flavor x during a given session. To eliminate the influence of side-biases mice were tested four consecutive times with sipper positions being switched between any two consecutive tests, with the overall average across trials defined as the actual preference.

Orofacial reactivity: Animals exposed to either intra-ileal or intra-oral infusions via catheters had orofacial reactions assessed as previously described (Travers et al., 2007). Videos were scored by a blinded observer. For head-fixed mice, the time of each occurrence of a facial movement falling into one of the following aversive categories was noted: lateral mouth movement, jaw chatter, mouth swipe, and gape. These response categories are like the oral reactivity responses that have been described in the literature (Travers et al., 2007), excepting the jaw-chatter. During this movement forceful closing of the jaw is accompanied by an un-subtle displacement of the ocular globe in the orbit. This response was seen frequently in response to bitter or strongly sour tastes, so was included here. Videos of animals' facial responses were recorded at 100 fps, individual frames were triggered using the recording equipment (TDT RZ5, which also triggered pumps for ileum infusion), and this allowed accurate measurement of time relative to the infusions.

Lick-triggered intra-ileal and intra-duodenal infusions: Mice were trained to produce licks to a metallic spout containing 5% IntraLipid to receive either intra-ileal or intra-

duodenal infusions of IntraLipid fat emulsions. The exterior part of the catheter was connected to a segment of MicroRenathane tubing secured to the tip of a 3mL standard syringe containing the solutions to be infused and mounted on the syringe pump. The syringe pump was placed near a small hole made on the superior part of the sound attenuating box in such a way that mice could move freely inside the behavioral chambers. During the task, 200 detected licks of 5% IntraLipid triggered a 180μL intra-ileal or intra-duodenal infusion of 20% IntraLipid that lasted for 6 seconds. However, licks detected while an infusion was taking place had no programmed consequences (i.e., did not result in additional infusions). Experimental tests lasted for 1 hour. Animals were tested once a day in their responses to one single concentration of IntraLipid (20%). Habituation sessions lasted for 1h and were performed daily allowing animals to lick water. Animals were considered trained to perform the experiments once they showed less than 10% between-session variability, a criterion reached within 10 consecutive sessions. In a variation of this task, animals were simply assessed for total licks to 5% IntraLipid. To generate IntraLipid lick data, we counted the total number of positive timestamps stored in the file containing the timestamps associated with licks detected by the contact lickometer (Med Associates). Thus, the IntraLipid lick data correspond to total numbers of detected licks during the 1-hour sessions.

Lick-triggered optogenetic stimulation over PSTn → PCRt: Implanted mice were connected to an opto-fiber cord and trained to produce licks to a metallic spout containing 2mM Sucralose. Training sessions lasted for one hour. Animals were considered trained to perform the experiments once they showed less than 10% between-session variability. During the one-hour test session, a detected lick triggered a TTL signal and turned the laser ON. Animal received a 25-ms 20 Hz laser pulse train stimulation lasted for 3 seconds. However, licks detected while an infusion was taking place had no programmed consequences (i.e., did not result in additional infusions). To generate the sucralose lick data, we counted the total number of positive timestamps stored in the file containing the timestamps associated with licks detected by the contact lickometer (Med Associates). Thus, the sucralose lick data correspond to total numbers of detected licks during the 1-hour sessions.

Food intake upon optogenetic stimulation over PSTn → PCRt: Mice were single caged and 2.5g chow/day food restricted. Implanted mice were connected to an opto-fiber cord and were allowed *ad libitum* access to chow in home-cage covered with open-top lid. After 1hour free consumption, the pellets were removed and weighted. Animals were considered trained to perform the experiments once they showed less than 10% between-session variability. During the one-hour test session, implanted mice were connected to an opto-fiber cord and were allowed *ad libitum* access to chow. At the same time, animals received a constant laser stimulation which was programed as 1-s long 25-ms 20 Hz laser pulse trains, with 2-s long intertrial intervals. The pellets were removed and weighted afterwards.

Online place preference and avoidance tests (optogenetics): Place preference tests made use of automated video analyses (EthoVision XT11.5, Noldus). A rat behavioral cage was prepared in such a way that the floor of one half of the cage was covered by bedding

(preferred by all mice) and the floor of the other half of the cage was covered by an acrylic platform (less preferred by all mice). To demonstrate place preferences, the less preferred area of the test cage was associated with switching the laser source ON, in such a way that the presence of the mouse in this area of the cage switched the laser source ON via a TTL board under control of the camera monitoring. To demonstrate place avoidance, the preferred area of the test cage was associated with switching the laser source ON. Quantification of occupancy of different areas of the cage made use of automated video analyses (EthoVision XT11.5, Noldus).

Optical stimulation regimens: Stimulation frequencies were chosen according to the outcome of the nerve or slice electrophysiological studies. Although we did not detect major differences between stimulation frequencies in terms of evoking (or failing to) behavior, we used the 25-ms 20Hz frequencies for VGlut2-positive parasubthalamic nucleus neurons and/or terminals. Intensity at tip of fibers was estimated at approximately 5mW.

Chemogenetic activation: Clozapine-N-Oxide (5mg/kg, EnZo Life Sciences) was injected *i.p.,* 15 mins before the start of the behavioral sessions.

Anatomical, electrophysiological, lesion, and optogenetic studies linking spinal transmission from stomach to brain: To determine the pathways via which stomach-innervating DRGs ("DRG[Stom]") signals distension to brain, we first performed gut-brain mapping in an organ-specific manner. We injected the retrograde *Cre*-expressing AAV2-retro-hSyn.HI.eGFP-Cre virus into the muscle layers of the stomach of wild-type mice, followed by bilateral injections of H129-CAG-LSL-TK-tdTomato into DRG[Stom] (T7-T10). In addition to DRGs and spinal cord, we analyzed and imaged HSV labeling in the lateral reticular formation ("LRN"), a medullary nucleus involved in decoding proprioceptive spinal signals (Pivetta et al., 2014). We also imaged HSV of DRG[Stom] origin detected most conspicuously in the parasubthalamic nucleus ("PSTn"), a lateral hypothalamic region involved in appetite suppression (Barbier et al., 2020). Tracing data are shown in Figures 5E and 5F and areas infected are listed in Table S1. We performed additional anatomical studies that revealed that NG[Stom] *versus* DRG[Stom] appear to access the lower brainstem via divergent pathways (see Figures S5I–S5O). The custom-built integrated system was the used to simultaneously acquire stomach electromyogram, single unit, and high-speed video records from head-fixed mice. The state of gastric distension was manipulated via the intra-gastric balloon. To confirm that PSTn is downstream of an ileal-hypothalamic pathway, we injected the *Cre*-dependent, polysynaptic retrograde virus PRV-2017 into the PSTn of VGlut2-ires-Cre mice (PSTn predominantly expresses excitatory VGlut2+ neurons; Barbier et al., 2020). Because VGlut2+ PSTn neurons (henceforth "PSTn[VGlut2]") were connected to upstream structures including LRN, thoracic DRGs, CG, and, importantly, GLP-1R+ ileal myenteric neurons we imaged these structures. We also performed single neuron electrophysiological recordings from PSTn of head-fixed mice implanted with an intra-gastric balloon to show that PSTn neurons respond to balloon inflation. To cell-specifically ablate excitatory PSTn[VGlut2] neurons, we injected the *Cre*-inducible caspase3 construct AAV5-flex-taCasp3 into the PSTn of VGlut2-ires-*Cre* mice. To explore the functional significance of the activation of PSTn neurons by intestinal GLP-1, we performed

electrophysiological recordings concomitant to electromyograms of jaw musculature and high-resolution video recordings for orofacial reactivity analyses. We monitored the display of rejection-like responses (Dolensek et al., 2020), including gaping and paw flaying.

To test that PSTn controls craniofacial motor systems, we injected the polysynaptic retrograde virus PRV into the masseter, digastric, and genioglossus muscles, and into the parotid gland, which respectively control jaw closing, opening, tongue protrusions, and salivary secretion (Han et al., 2017). The targeted muscles are critical for the generation of rejection motor responses (Travers and Norgren, 1986). We imaged well localized labeling of PSTn neurons after injections into masseter and, more conspicuously, digastric and genioglossus. PRV injections were also performed into salivary glands and labeling in PSTn was imaged. Moreover, we injected the *Cre*-dependent, polysynaptic retrograde virus PRV-2017 into the PSTn of VGlut2-ires-*Cre* mice, and imaged neuron labeling in taste buds and geniculate ganglia (Barretto et al., 2015).

Finally, because forebrain regions access the trigeminal motor nucleus via the pontine parvocellular reticular formation ("PCRt"; Han et al., 2017), we studied $PSTn^{VGlut2}$ ->PCRt pathways using optogenetics. Tofunctionally target $PSTn^{VGlut2}$ neurons, we injected the depolarizing optogenetic construct AAV5-EF1a-DIO-hChR2[H134R]-EYFP into the PSTn of VGlut2-ires-Cre mice. This idea was based on detection of synaptophisin EYFP+ terminals in PCRt (see Figure 7K). We thus implanted optical fibers over PCRt in these animals.

QUANTIFICATION AND STATISTICAL ANALYSIS

Data analyses, excluding electromyogram/electrophysiological/calcium imaging data, were performed using SPSS (v.21.0, IBM Predictive Software), Ethovision XT 11.5 (Noldus), GraphPad Prism 7 (GraphPad) and Matlab (v.17b, MathWorks). Animals assigned to the different experimental groups were experimentally naive littermates, so that no randomization or other a priori criteria were adopted for group assignments. Experimental manipulations were analyzed according to within-subject repeated-measures designs. Order of experimental conditions was randomly assigned across subjects. Samples sizes were chosen based on our previous studies employing similar optogenetic, electrophysiological and neuronal ablation approaches. Samples sizes adopted in our current study were sufficient for detecting strong effect sizes while complying with guidelines from local enforcing rules requesting minimal animal usage by our Institutional Animal Care and Use Committee. Experimenters were not blind to experimental conditions. Only animals carrying signs of distress/infection/bleeding/anorexia after the surgical procedures were excluded. Data from all animals used in the experiments were included in the final analyses and plots.

Analysis of behavioral trials—For all behavioral studies, including those resulting from pathway-targeted lesions, optogenetics and/or chemogenetic experiments, analyses made use of standard linear models (Pearson correlation), as well as one- or two-way (repeated measures) ANOVAs and post-hoc t-tests tests whenever relevant, for correcting for multiple comparisons. All data were reported as mean±SEM. In all cases sample sizes (N) denote number of animals used. All p-values associated with the t-tests performed

correspond to two-tailed tests, and all post-hoc tests were corrected for multiple comparisons by employing Bonferroni correction. To assess potentially spurious results associated with non-normality, all significant effects were confirmed by rerunning the tests using the appropriate non-parametric test. All data are individually plotted (Prism 7, GraphPad), and the corresponding bar plot of the precision measures (mean ± SEM) were overlaid on the figure. The exact value of all N (always number of animals), df, T/F, and p values are reported in the figure legends. An effect was considered statistically significant whenever the corresponding statistic was associated with a p-value (Bonferroni-corrected when appropriate) strictly less than 0.05.

Calcium imaging data analysis—The raw data from calcium transients were first motion-corrected using NoRMCorre (Pnevmatikakis and Giovannucci, 2017). The data were then denoised using DeepCAD, a self-supervised deep-learning method for spatiotemporal enhancement of calcium imaging data (Li et al., 2021). Overall number of training epochs was 7–9. We then generated the maximum intensity projection of the time-lapse images and utilized Cellpose, a deep learning-based segmentation method (Stringer et al., 2021), to segment individual neurons. The output files corresponding to each region of interest (ROIs) of individual neurons were stored as an ImageJ ROI file.

Using the motion-corrected imaging data and segmentation ROI files, we then calculated the mean values of both ROI GCaMP signals (ROI-Signal$_{Mean}$) and of the surrounding background (Background-Signal$_{Mean}$) for each individual neuron, following the strategy of the CaImAn software package (Giovannucci et al., 2019; Pnevmatikakis and Giovannucci, 2017). The calcium signal of each neuron was then defined as ROI-Signal$_{Mean}$ - Background-Signal$_{Mean}$. We next computed, for each neuron, calcium signal z-scores using the mean values and standard deviations obtained from 5 min-long baseline periods observed before GLP-1 infusions into the ileum. The *Python*-based packages used for data analysis included NumPy (version 1.22.0), SciPy (version 1.7.1), Pandas (version 1.4.1), Matplotlib (version 3.4.3), and Seaborn (version 0.11.2).

Analysis of electrophysiology data

Determination of unit response following ileum infusions: To score unit responses to infusion of IntraLipid, GLP-1, or control solutions into the ileum, we devised a threshold-based criteria that could be applied to a design where only a single infusion of the control and of the experimental solution are performed. This was done for two reasons. First, the response to infusions of these substances (both behavioral and electrophysiological) took at least 10 minutes to develop and persisted for more than an hour. This was considered too long to perform multiple trials in a head fixed animal. Second, repeated infusions would raise the substantial confound of additive effects to multiple infusions.

To quantify the response of single units to ileum infusions, a principal component approach was adopted. Single units' firing rates were discretized into 2–5 second bins. Firing rates were Z-transformed, and the principal components of the transformed rates of all recorded units in response to the experimental infusion were calculated. For each unit, the weight or score of the first principal component was taken as its response to the experimental

infusion. To set a threshold for determining which responses were significant, for each cell, its transformed firing rate in response to the control infusion was dot-multiplied with the first principal component calculated from the population response to the experimental infusion. In the resulting distribution, 3 standard deviations above the mean were set as a threshold value. A given unit was considered respondent to the ileal stimulus if the unit's principal component 1 score in response to the experimental infusion that was greater than 3 standard deviations above the mean.

Determination of single-neuron responses to stomach balloon inflation: Firing rates were discretized to 5 second bins and Z-transformed. Three trials of balloon inflation and deflation were performed for each cell. A trial consisted of a balloon inflation-deflation program, as well as a period 20 seconds before and 20 seconds after the program. For PSTn recordings, the balloon was inflated to 0.3mL volume over 40 seconds, then deflated at the same rate. For LRN recordings the balloon was inflated to 0.5mL over 40 seconds, then deflated. For each cell, the trails were pooled, and Pearson's correlation coefficient was calculated between the cell's firing rate and the balloon volume. P-values were separately corrected (Holm-Sidak) for each recording area, and those meeting the cut-off were determined to be correlated to the balloon volume.

Construction of EMG-based rasters: Rasters of cells recorded in the LRN were created based on bursts of contractions in the stomach EMG signal. To determine contraction events for constructing the raster, EMG traces from the stomach were integrated offline by high pass Altering at 300–500 Hz, then rectifying, and convolving with a 0.1 second boxcar. This integrated trace was Z-transformed, and a threshold for peak prominence was determined by manual oversight. The occurrence of a peak in this trace, separated by at least 1 second from surrounding peaks, was included as an event for an EMG triggered raster.

Cell firing rates were discretized into 0.1 second bins, and Z transformed. Cells that showed a significant difference in their firing rate during three periods relative initiation of EMG activity were determined to be significantly modulated in concert with the stomach. Specifically, the periods considered were as follows: pre-spanning from 10 to 9 seconds before the EMG event; peri-spanning from 0–1 seconds immediately after the EMG event; post-spanning from 9–10 seconds after the EMG event. Using a Friedman test, cells having significantly different rates between these periods were considered EMG modulated.

In a subset of experiments, simultaneous measurement of overlaying abdominal EMG and pylorus EMG signal provided reasonable assurance that the EMG signal for the corpus had minimal crosstalk between the overlaying skeletal muscle, and that high pass filtering substantially minimized movement related artifacts.

Spike sorting was performed manually using offlinesorter (Plexon). Data were then imported into Matlab or Python for analysis using custom-written software. Code for analysis is available upon request.

To perform EMG analyses, the signals were full-wave rectified and root mean square (RMS)-converted within moving windows of 25-ms duration. Baseline signals (obtained

from those periods during which the laser source was off) were used to establish a cut-off C_{off} value defined by the overall session mean M_S and associated standard deviation STD_S of the signals as

$$C_{off} = M_S + (3 \times STD_S)$$

This cut off value was then used to determine whether the signal (S) at a given time point was significantly different from baseline *(i.e. $S \geq C_{off}$)*. Each time point in which this inequality holds true were defined as an "event". These analyses were performed using custom software programmed in MATLAB (v.17b, MathWorks) and are available upon request.

Supplementary Material

Refer to Web version on PubMed Central for supplementary material.

ACKNOWLEDGMENTS

REFERENCES

Bai L, Mesgarzadeh S, Ramesh KS, Huey EL, Liu Y, Gray LA, Aitken TJ, Chen Y, Beutler LR, Ahn JS, et al. (2019). Genetic identification of vagal sensory neurons that control feeding. Cell 179, 1129–1143.e23. [PubMed: 31730854]

Barbier M, Chometton S, Pautrat A, Miguet-Alfonsi C, Datiche F, Gascuel J, Fellmann D, Peterschmitt Y, Coizet V, and Risold PY (2020). A basal ganglia-like cortical-amygdalar-hypothalamic network mediates feeding behavior. Proc. Natl. Acad. Sci. USA 117, 15967–15976. [PubMed: 32571909]

Barretto RP, Gillis-Smith S, Chandrashekar J, Yarmolinsky DA, Schnitzer MJ, Ryba NJ, and Zuker CS (2015). The neural representation of taste quality at the periphery. Nature 517, 373–376. [PubMed: 25383521]

Berthoud HR, Blackshaw LA, Brookes SJ, and Grundy D. (2004). Neuroanatomy of extrinsic afferents supplying the gastrointestinal tract. Neurogastroenterol. Motil 16, 28–33. [PubMed: 15066001]

Berthoud HR, and Powley TL (1992). Vagal afferent innervation of the rat fundic stomach: morphological characterization of the gastric tension receptor. J. Comp. Neurol 319, 261–276. [PubMed: 1522247]

Blackshaw LA, Brookes SJ, Grundy D, and Schemann M. (2007). Sensory transmission in the gastrointestinal tract. Neurogastroenterol. Motil19, 1–19.

Borgmann D, Ciglieri E, Biglari N, Brandt C, Cremer AL, Backes H, Tittgemeyer M, Wunderlich FT, Brüning JC, and Fenselau H. (2021). Gutbrain communication by distinct sensory neurons differently controls feeding and glucose metabolism. Cell Metab. 33, 1466–1482.e7. [PubMed: 34043943]

Brierley DI, Holt MK, Singh A, de Araujo A, McDougle M, Vergara M, Afaghani MH, Lee SJ, Scott K, Maske C, et al. (2021). Central and peripheral GLP-1 systems independently suppress eating. Nat. Metab 3, 258–273. [PubMed: 33589843]

Brokhman I, Xu J, Coles BLK, Razavi R, Engert S, Lickert H, Babona-Pilipos R, Morshead CM, Sibley E, Chen C, et al. (2019). Dual embryonic origin of the mammalian enteric nervous system. Dev. Biol 445, 256–270. [PubMed: 30472119]

Burcelin R, Serino M, and Cabou C. (2009). A role for the gut-to-brain GLP-1-dependent axis in the control of metabolism. Curr. Opin. Pharmacol 9, 744–752. [PubMed: 19800290]

Burmeister MA, Ayala JE, Smouse H, Landivar-Rocha A, Brown JD, Drucker DJ, Stoffers DA, Sandoval DA, Seeley RJ, and Ayala JE (2017). The hypothalamic glucagon-like peptide 1 receptor is sufficient but not necessary for the regulation of energy balance and glucose homeostasis in mice. Diabetes 66, 372–384. [PubMed: 27908915]

Camilleri M, Chedid V, Ford AC, Haruma K, Horowitz M, Jones KL, Low PA, Park SY, Parkman HP, and Stanghellini V. (2018). Gastroparesis. Nat. Rev. Dis. Primers 4, 41. [PubMed: 30385743]

Cannon WB, and Washburn AL (1993). An explanation of hunger. 1911.Obes. Res 1, 494–500. [PubMed: 16350324]

Chambers AP, Sorrell JE, Haller A, Roelofs K, Hutch CR, Kim KS, Gutierrez-Aguilar R, Li B, Drucker DJ, D'Alessio DA, et al. (2017). The role of pancreatic preproglucagon in glucose homeostasis in mice. Cell Metab.25, 927–934.e3. [PubMed: 28325479]

Corsetti M, Gevers AM, Caenepeel P, and Tack J. (2004). The role of tension receptors in colonic mechanosensitivity in humans. Gut 53, 1787–1793. [PubMed: 15542515]

Craig AD (2002). How do you feel? Interoception: the sense of the physiological condition of the body. Nat. Rev. Neurosci 3, 655–666. [PubMed: 12154366]

Dailey MJ, and Moran TH (2013). Glucagon-like peptide 1 and appetite. Trends Endocrinol. Metab 24, 85–91. [PubMed: 23332584]

D'Alessio D. (2016). Is GLP-1 a hormone: whether and When? J. Diabetes Investig 7, 50–55.

Deacon CF (2005). What do we know about the secretion and degradation of incretin hormones? Regul. Pept 128, 117–124. [PubMed: 15780431]

Dolensek N, Gehrlach DA, Klein AS, and Gogolla N. (2020). Facial expressions of emotion states and their neuronal correlates in mice. Science 368, 89–94. [PubMed: 32241948]

Drucker DJ (2018). Mechanisms of action and therapeutic application of glucagon-like peptide-1. Cell Metab. 27, 740–756. [PubMed: 29617641]

Eissele R, Göke R, Willemer S, Harthus HP, Vermeer H, Arnold R, and Göke B. (1992). Glucagon-like peptide-1 cells in the gastrointestinal tract and pancreas of rat, pig and man. Eur. J. Clin. Invest 22, 283–291. [PubMed: 1499644]

Furness JB (2006). Novel gut afferents: intrinsic afferent neurons and intestinofugal neurons. Auton. Neurosci 125, 81–85. [PubMed: 16476573]

Furness JB, Callaghan BP, Rivera LR, and Cho HJ (2014). The enteric nervous system and gastrointestinal innervation: integrated local and central control. Adv. Exp. Med. Biol 817, 39–71. [PubMed: 24997029]

Giovannucci A, Friedrich J, Gunn P, Kalfon J, Brown BL, Koay SA, Taxidis J, Najafi F, Gauthier JL, Zhou P, et al. (2019). CaImAn an open source tool for scalable calcium imaging data analysis. eLife 8, e38173.

Giralt M, and Vergara P. (1999). Glucagonlike peptide-1 (GLP-1) participation in ileal brake induced by intraluminal peptones in rat. Dig. Dis. Sci 44, 322–329. [PubMed: 10063918]

Grasset E, Puel A, Charpentier J, Collet X, Christensen JE, Tercé F, and Burcelin R. (2017). A specific gut microbiota dysbiosis of type 2 diabetic mice induces GLP-1 resistance through an enteric NO-dependent and gut-brain axis mechanism. Cell Metab. 25, 1075–1090.e5. [PubMed: 28467926]

Han W, and de Araujo IE (2021). Dissection and surgical approaches to the mouse jugular-nodose ganglia. Star Protoc. 2, 100474. [PubMed: 33997807]

Han W, Tellez LA, Perkins MH, Perez IO, Qu T, Ferreira J, Ferreira TL, Quinn D, Liu ZW, Gao XB, et al. (2018). A neural circuit for gut-induced reward. Cell 175, 665–678.e623. [PubMed: 30245012]

Han W, Tellez LA, Rangel MJ Jr., Motta SC, Zhang X, Perez IO, Canteras NS, Shammah-Lagnado SJ, van den Pol AN, and de Araujo IE (2017). Integrated control of predatory hunting by the central nucleus of the amygdala. Cell 168, 311–324.e18. [PubMed: 28086095]

Hansen L, Deacon CF, Orskov C, and Holst JJ (1999). Glucagon-like peptide-1-(7–36)amide is transformed to glucagon-like peptide-1-(9–36)amide by dipeptidyl peptidase IV in the capillaries supplying the L cells of the porcine intestine. Endocrinology 140, 5356–5363. [PubMed: 10537167]

Herrmann-Rinke C, Vöge A, Hess M, and Göke B. (1995). Regulation of glucagon-like peptide-1 secretion from rat ileum by neurotransmitters and peptides. J. Endocrinol 147, 25–31. [PubMed: 7490533]

Hibberd TJ, Yew WP, Chen BN, Costa M, Brookes SJ, and Spencer NJ (2020). A novel mode of sympathetic reflex activation mediated by the enteric nervous system. eNeuro 7. ENEURO.0187–20.2020.

Holst JJ (2007). The physiology of glucagon-like peptide 1. Physiol. Rev 87, 1409–1439. [PubMed: 17928588]

Holst JJ, Andersen DB, and Grunddal KV (2022). Actions of glucagon-like peptide-1 receptor ligands in the gut. Br. J. Pharmacol 179, 727–742. [PubMed: 34235727]

Iggo A. (1955). Tension receptors in the stomach and the urinary bladder. J. Physiol 128, 593–607. [PubMed: 13243351]

Jares-Erijman EA, and Jovin TM (2003). FRET imaging. Nat. Biotechnol 21, 1387–1395. [PubMed: 14595367]

Jessen L, Aulinger BA, Hassel JL, Roy KJ, Smith EP, Greer TM, Woods SC, Seeley RJ, and D'Alessio DA (2012). Suppression of food intake by glucagon-like peptide-1 receptor agonists: relative potencies and role of dipeptidyl peptidase-4. Endocrinology 153, 5735–5745. [PubMed: 23033273]

Kanoski SE, Hayes MR, and Skibicka KP (2016). GLP-1 and weight loss: unraveling the diverse neural circuitry. Am. J. Physiol. Regul. Integr. Comp.Physiol 310, R885–R895. [PubMed: 27030669]

Keast JR, and De Groat WC (1992). Segmental distribution and peptide content of primary afferent neurons innervating the urogenital organs and colon of male rats. J. Comp. Neurol 319, 615–623. [PubMed: 1619047]

Kim DH, D'Alessio DA, Woods SC, and Seeley RJ (2009). The effects of GLP-1 infusion in the hepatic portal region on food intake. Regul. Pept 155, 110–114. [PubMed: 19289143]

Kim DY, Heo G, Kim M, Kim H, Jin JA, Kim HK, Jung S, An M, Ahn BH, Park JH, et al. (2020). A neural circuit mechanism for mechanosensory feedback control of ingestion. Nature 580, 376–380. [PubMed: 32296182]

Layer P, Holst JJ, Grandt D, and Goebell H. (1995). Ileal release of glucagon-like peptide-1 (GLP-1). Association with inhibition of gastric acid secretion in humans. Dig. Dis. Sci 40, 1074–1082. [PubMed: 7729267]

Lebrun LJ, Lenaerts K, Kiers D, Pais de Barros JP, Le Guern N, Plesnik J, Thomas C, Bourgeois T, Dejong CHC, Kox M, et al. (2017). Enteroendocrine L cells sense LPS after gut barrier injury to enhance GLP-1 secretion. Cell Rep. 21, 1160–1168. [PubMed: 29091756]

Li X, Zhang G, Wu J, Zhang Y, Zhao Z, Lin X, Qiao H, Xie H, Wang H, Fang L, and Dai Q. (2021). Reinforcing neuron extraction and spike inference in calcium imaging using deep self-supervised denoising. Nat. Methods 18, 1395–1400. [PubMed: 34400836]

Lo L, and Anderson DJ (2011). A Cre-dependent, anterograde transsynaptic viral tracer for mapping output pathways of genetically marked neurons. Neuron 72, 938–950. [PubMed: 22196330]

Lund ML, Sorrentino G, Egerod KL, Kroone C, Mortensen B, Knop FK, Reimann F, Gribble FM, Drucker DJ, de Koning EJP, et al. (2020). L-cell differentiation is induced by bile acids through GPBAR1 and paracrine GLP-1 and serotonin signaling. Diabetes 69, 614–623. [PubMed: 32041793]

Lynn PA, Olsson C, Zagorodnyuk V, Costa M, and Brookes SJ (2003). Rectal intraganglionic laminar endings are transduction sites of extrinsic mechanoreceptors in the guinea pig rectum. Gastroenterology 125, 786–794. [PubMed: 12949724]

Meier JJ, Kemmeries G, Holst JJ, and Nauck MA (2005). Erythromycin antagonizes the deceleration of gastric emptying by glucagon-like peptide 1 and unmasks its insulinotropic effect in healthy subjects. Diabetes 54, 2212–2218. [PubMed: 15983224]

Merrill L, Gonzalez EJ, Girard BM, and Vizzard MA (2016). Receptors, channels, and signalling in the urothelial sensory system in the bladder. Nat.Rev. Urol 13, 193–204. [PubMed: 26926246]

Milstein JA, Lehmann O, Theobald DE, Dalley JW, and Robbins TW (2007). Selective depletion of cortical noradrenaline by anti-dopamine beta-hydroxylase-saporin impairs attentional function and enhances the effects of guanfacine in the rat. Psychopharmacol. (Berl.) 190, 51–63.

Muller PA, Schneeberger M, Matheis F, Wang P, Kerner Z, Ilanges A, Pellegrino K, Del Mármol J, Castro TBR, Furuichi M, et al. (2020). Microbiota modulate sympathetic neurons via a gut-brain circuit. Nature 583, 441–446. [PubMed: 32641826]

Müller TD, Finan B, Bloom SR, D'Alessio D, Drucker DJ, Flatt PR, Fritsche A, Gribble F, Grill HJ, Habener JF, et al. (2019). Glucagon-like peptide 1 (GLP-1). Mol. Metab 30, 72–130. [PubMed: 31767182]

Nauck MA, Niedereichholz U, Ettler R, Holst JJ, Orskov C, Ritzel R, and Schmiegel WH (1997). Glucagon-like peptide 1 inhibition of gastric emptying outweighs its insulinotropic effects in healthy humans. Am. J. Physiol 273, E981–E988. [PubMed: 9374685]

Panaro BL, Yusta B, Matthews D, Koehler JA, Song Y, Sandoval DA, and Drucker DJ (2020). Intestine-selective reduction of Gcg expression reveals the importance of the distal gut for GLP-1 secretion. Mol. Metab 37, 100990.

Paternoster S, and Falasca M. (2018). Dissecting the physiology and pathophysiology of glucagon-like peptide-1. Front. Endocrinol. (Lausanne) 9, 584. [PubMed: 30364192]

Pivetta C, Esposito MS, Sigrist M, and Arber S. (2014). Motor-circuit communication matrix from spinal cord to brainstem neurons revealed by developmental origin. Cell 156, 537–548. [PubMed: 24485459]

Plamboeck A, Veedfald S, Deacon CF, Hartmann B, Wettergren A, Svendsen LB, Meisner S, Hovendal C, Vilsbøll T, Knop FK, and Holst JJ (2013). The effect of exogenous GLP-1 on food intake is lost in male truncally vagotomized subjects with pyloroplasty. Am. J. Physiol. Gastrointest. Liver Physiol 304, G1117–G1127. [PubMed: 23599045]

Pnevmatikakis EA, and Giovannucci A. (2017). NoRMCorre: an online algorithm for piecewise rigid motion correction of calcium imaging data. J. Neurosci. Methods 291, 83–94. [PubMed: 28782629]

Pnevmatikakis EA, Soudry D, Gao Y, Machado TA, Merel J, Pfau D, Reardon T, Mu Y, Lacefield C, Yang W, et al. (2016). Simultaneous Denoising, Deconvolution, and Demixing of Calcium Imaging Data. Neuron 89, 285–299. [PubMed: 26774160]

Punjabi M, Arnold M, Geary N, Langhans W, and Pacheco-López G. (2011). Peripheral glucagon-like peptide-1 (GLP-1) and satiation. Physiol. Behav 105, 71–76. [PubMed: 21371486]

Rakhilin N, Garrett A, Eom CY, Chavez KR, Small DM, Daniel AR, Kaelberer MM, Mejooli MA, Huang Q, Ding S, et al. (2019). An intravital window to image the colon in real time. Nat. Commun 10, 5647. [PubMed: 31827103]

Read NW, McFarlane A, Kinsman RI, Bates TE, Blackhall NW, Farrar GB, Hall JC, Moss G, Morris AP, O'Neill B, et al. (1984). Effect of infusion of nutrient solutions into the ileum on gastrointestinal transit and plasma levels of neurotensin and enteroglucagon. Gastroenterology 86, 274–280. [PubMed: 6690354]

Renier N, Wu Z, Simon DJ, Yang J, Ariel P, and Tessier-Lavigne M. (2014). iDISCO: a simple, rapid method to immunolabel large tissue samples for volume imaging. Cell 159, 896–910. [PubMed: 25417164]

Ritzel U, Fromme A, Ottleben M, Leonhardt U, and Ramadori G. (1997). Release of glucagon-like peptide-1 (GLP-1) by carbohydrates in the perfused rat ileum. Acta Diabetol. 34, 18–21. [PubMed: 9134052]

Robinson PH, McHugh PR, Moran TH, and Stephenson JD (1988). Gastric control of food intake. J. Psychosom. Res 32, 593–606. [PubMed: 3065484]

Rotondo A, Amato A, Lentini L, Baldassano S, and Mulè F. (2011). Glucagon-like peptide-1 relaxes gastric antrum through nitric oxide in mice. Peptides 32, 60–64. [PubMed: 20933560]

Rüttimann EB, Arnold M, Hillebrand JJ, Geary N, and Langhans W. (2009). Intrameal hepatic portal and intraperitoneal infusions of glucagon-like peptide-1 reduce spontaneous meal size in the rat via different mechanisms. Endocrinology 150, 1174–1181. [PubMed: 18948395]

Schirra J, and Göke B. (2005). The physiological role of GLP-1 in human: incretin, ileal brake or more? Regul. Pept 128, 109–115. [PubMed: 15780430]

Schmidt WE, Siegel EG, and Creutzfeldt W. (1985). Glucagon-like peptide-1 but not glucagon-like peptide-2 stimulates insulin release from isolated rat pancreatic islets. Diabetologia 28, 704–707. [PubMed: 3905480]

Song Y, Koehler JA, Baggio LL, Powers AC, Sandoval DA, and Drucker DJ (2019). Gut-proglucagon-derived peptides are essential for regulating glucose homeostasis in mice. Cell Metab. 30, 976–986.e3. [PubMed: 31495689]

Spencer NJ, Zagorodnyuk V, Brookes SJ, and Hibberd T. (2016). Spinal afferent nerve endings in visceral organs: recent advances. Am. J. Physiol.Gastrointest. Liver Physiol 311, G1056–G1063. [PubMed: 27856418]

Sternson SM, and Roth BL (2014). Chemogenetic tools to interrogate brain functions. Annu. Rev. Neurosci 37, 387–407. [PubMed: 25002280]

Stringer C, Wang T, Michaelos M, and Pachitariu M. (2021). Cellpose: a generalist algorithm for cellular segmentation. Nat. Methods 18, 100–106. [PubMed: 33318659]

Szurszewski JH, Ermilov LG, and Miller SM (2002). Prevertebral ganglia and intestinofugal afferent neurones. Gut 51, i6–i10. [PubMed: 12077055]

Tack J, Talley NJ, Camilleri M, Holtmann G, Hu P, Malagelada JR, and Stanghellini V. (2006). Functional gastroduodenal disorders. Gastroenterology 130, 1466–1479. [PubMed: 16678560]

Tong J, and D'Alessio D. (2014). Give the receptor a brake: slowing gastric emptying by GLP-1. Diabetes 63, 407–409. [PubMed: 24464721]

Travers JB, Herman K, Yoo J, and Travers SP (2007). Taste reactivity and Fos expression in GAD1-EGFP transgenic mice. Chem. Senses 32, 129–137. [PubMed: 17082515]

Travers JB, and Norgren R. (1986). Electromyographic analysis of the ingestion and rejection of sapid stimuli in the rat. Behav. Neurosci 100, 544–555. [PubMed: 3741605]

Umans BD, and Liberles SD (2018). Neural sensing of organ volume. Trends Neurosci. 41, 911–924. [PubMed: 30143276]

Vahl TP, Tauchi M, Durler TS, Elfers EE, Fernandes TM, Bitner RD, Ellis KS, Woods SC, Seeley RJ, Herman JP, and D'Alessio DA (2007). Glucagon-like peptide-1 (GLP-1) receptors expressed on nerve terminals in the portal vein mediate the effects of endogenous GLP-1 on glucose tolerance in rats. Endocrinology 148, 4965–4973. [PubMed: 17584962]

Varin EM, Mulvihill EE, Baggio LL, Koehler JA, Cao X, Seeley RJ, and Drucker DJ (2019). Distinct neural sites of GLP-1R expression mediate physiological versus pharmacological control of incretin action. Cell Rep. 27, 3371–3384.e3. [PubMed: 31189118]

Vilsbøll T, Krarup T, Deacon CF, Madsbad S, and Holst JJ (2001). Reduced postprandial concentrations of intact biologically active glucagon-like peptide 1 in type 2 diabetic patients. Diabetes 50, 609–613. [PubMed: 11246881]

Williams EK, Chang RB, Strochlic DE, Umans BD, Lowell BB, and Liberles SD (2016). Sensory neurons that detect stretch and nutrients in the digestive system. Cell 166, 209–221. [PubMed: 27238020]

Windeløv JA, Wewer Albrechtsen NJ, Kuhre RE, Jepsen SL, Hornburg D, Pedersen J, Jensen EP, Galsgaard KD, Winther-Sørensen M, Ørgaard A, et al. (2017). Why is it so difficult to measure glucagon-like peptide-1 in a mouse? Diabetologia 60, 2066–2075. [PubMed: 28669086]

Zhang C, Kaye JA, Cai Z, Wang Y, Prescott SL, and Liberles SD (2021). Area postrema cell types that mediate nausea-associated behaviors. Neuron 109, 461–472.e5. [PubMed: 33278342]

Highlights

- Rather than a circulating hormone, endogenous GLP-1 acts on ileal enteric neurons

- Myenteric intestinofugal neurons mediate gastric and anorectic effects of GLP-1

- Nitric oxide gastric neurons are critical regulators of gastric distension and appetite

- Gastric volume is sensed by hypothalamic neurons via spinal afferent pathways
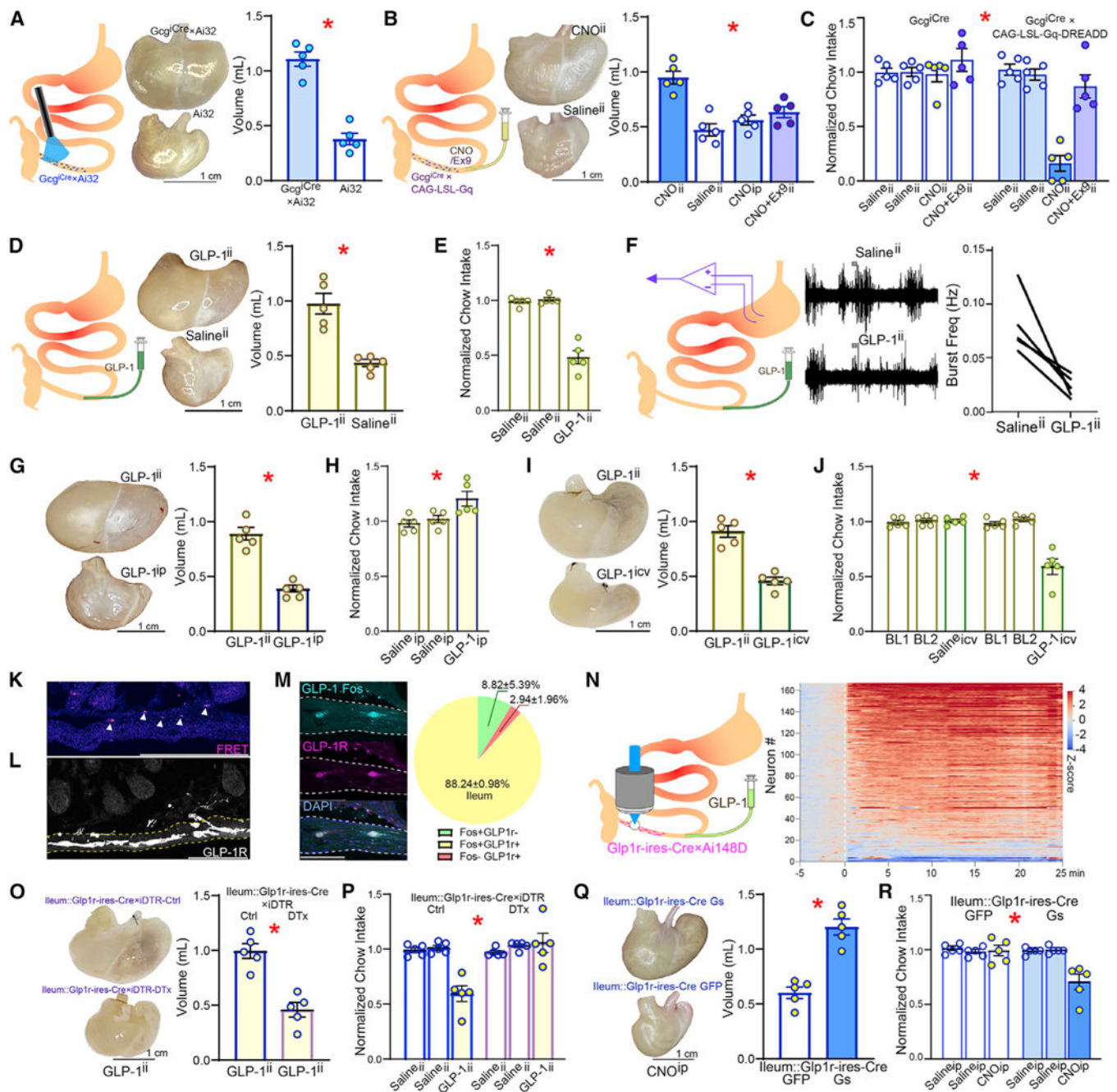
Figure 1. Gastric distension and appetite loss induced by ileal GLP-1 signaling

(A) After implanting an abdominal glass window, a blue laser beam was directed to the terminal ileum for *in vivo* optogenetic stimulation of the L cells in Gcg^{iCre}×Ai32 mice (left). Stimulation induced marked gastric distension in Gcg^{iCre}×Ai32. Middle: representative dissected stomachs; right: volumes of dissected stomachs; 2-sample t test $T(8) = 8.828$, * $p < 0.001$.

(B) CNO was infused via a catheter into terminal ileum (CNO^{ii}) for chemogenetic stimulation of L cells in Gcg^{iCre}×CAG-LSL-Gq mice (left), which caused marked gastric distension. Middle: representative dissected stomachs; right: volumes of dissected stomachs.

Neither Saline[ii] nor intra-peritoneal CNO (CNO[ip]) induced gastric distension, with CNO[ii] effects being blocked by concomitant intra-ileal infusions of the GLP-1R antagonist Exendin(9–39) (Ex-9[ii]); one-way ANOVA, injections × group $F_{(3,16)} = 15.474$, *p < 0.001. Bonferroni post hocs: (CNO[ii] versus Saline[ii], p < 0.001); (CNO[ii] versus CNO[ip], p = 0.001); (CNO[ii] versus CNO+Ex9[ii], p = 0.004).

(C) Within-subject design for daily measures of 1 h-food intake in food-restricted Gcg[iCre]×CAG-LSL-Gq mice. Two consecutive days of Saline[ii] are shown to demonstrate baseline stability. Although CNO[ii] caused marked reductions in food intake, the effect was completely abolished by concomitant Ex9[ii]; two-way RM-ANOVA, injections $F_{(1,8)} = 4.124$, p = 0.077; group $F_{(1,8)} = 30.26$, * p = 0.001, injections × group $F_{(1,8)} = 11.86$, * p = 0.009.

(D) Intra-ileal infusions of GLP-1 (GLP-1[ii]; 50 pmol/kg) in wild-type mice distended gastric volumes by ~100% compared with Saline[ii]; left: representative dissected stomachs; right: volume of dissected stomach; 2-sample t test $T_{(8)} = 5.417$,* p = 0.001.

(E) GLP-1[ii] decreases food intake by ~50% over 1 h, one-way RM-ANOVA $F_{(2,8)} = 60.756$, * p < 0.001.

(F) GLP-1[ii] suppresses stomach contractions. Left: Representative traces of EMG obtained from stomach following Saline[ii] or GLP-1[ii]. Right: aggregate data of average frequency of EMG bursts quantified over 5 min, beginning 10 min after completing ileal infusions (20 pmol/kg, 220 μL over 1 min); Paired t test, $T_{(4)} = 3.93$, * p = 0.0171.

(G) GLP-1[ii] but not GLP-1[ip] expands gastric volumes; t test $T_{(8)} = 7.764$, * p < 0.001.

(H) GLP-1[ip] did not affect 1 h-food intake, one-way RM-ANOVA $F_{(2,8)} = 5.617$, p = 0.077.

(I) GLP-1[ii] but not GLP-1[icv] expands gastric volumes; 2-sample t test $T_{(8)} = 7.189$,* p < 0.001.

(J) GLP-1[icv] also decreased food intake over 1 h, two-way RM-ANOVA; infusate × injection site: $F_{(2,16)} = 22.040$, * p < 0.001.

(K) Intact GLP-1 Förster resonance energy transfer (FRET) signals were detected in the ileal villi and submucosa (arrowheads).

(L) In GLP-1R-ires-Cre×Ai9 mice, myenteric GLP-1R+ fibers extended to the ileal submucosal layer, where intra-ileum infused GLP-1 was detected by FRET.

(M) GLP-1[ii] induced neuronal Fos expression in the majority (~88%) of GLP-1R+ neurons in the ileum (in parentheses are shown the numbers of cells per mm^2).

(N) Left: intravital imaging of ileal GLP-1R+ neuronal activity in Ai148D3GLP-1R-ires-Cre mice. GLP-1[ii] induced fast and sustained calcium transients in the ileal GLP-1R+ neurons. Right: heatmap of Z scores calculated with respect to baseline. T = 0 min: GLP-1[ii] infusion.

(O) Ileal infusions of diphtheria toxin (DTx) were employed to ablate ileal GLP-1R+ neurons in Glp1r-iresCre3iDTR mice. DTx-induced ablation of ileal GLP-1R+ neurons disrupted the gastric distension effects of GLP-1[ii]; 2-sample t test $T_{(8)} = 5.691$, * p < 0.001.

(P) Same as in (O) but for within-subject measures of daily 1 h-feeding in saline and DTx groups; two-way mixed RM-ANOVA, infusate × group: $F_{(2,16)} = 14.306$, * p < 0.001.

(Q) The excitatory chemogenetic construct AAVdj-DIO-Gs-mCherry was injected into the ileum of Glp1r-ires-Cre mice (GLP-1R-Gs). Control Glp1r-ires-Cre micewere injected with AAVdj-DIO-mCherry (GLP-1R-Ctrl). Chemogenetic activation-induced significant stomach distensions; left: representative dissected stomachs; right: volume of dissected stomachs; 2-sample t test $T_{(8)} = 6.651$, * p < 0.001.

(R) As in (Q), but for within-subject measures of daily 1 h-feeding. Chemogenetic activation of ileal GLP-1R+ neurons mimics appetite suppression by GLP-1[ii] over 1 h. Two-way mixed RM-ANOVA, injection $\times$ group $F(2,16) = 9.232$, * $p = 0.002$. Data are represented as mean $\pm$ SEM in all figures.

See also Figure S1.

Figure 2. Ileal GLP-1 effects are mediated by intestinofugal neurons

(A) GLP-1^{ii} induces neuronal Fos expression in celiac ganglia (CG), 2-sample t test, T(8) = 5.496, *p < 0.001.

(B) Chemogenetic activation of ileal GLP-1R+ neurons performed as in Figure 1Q. Chemogenetic activation triggers Fos in CG. Left: mCherry+ terminals from DREADD-expressing GLP-1R+ ileal neurons innervating CG. Middle: Fos+ counts, 2-sample t test, T(8) = 5.496, * p < 0.001.

(C) (i) The retrograde, *Cre*-expressing construct AAVrg-Cre was injected into celiac ganglia (CG) of Ai9 mice for visualization of intestinofugal neurons (IFNs). (ii–iii) Large IFNs and their extensive projections were visualized in the myenteric layer of the terminal ileum. (iv) Processes arising from ileal IFNs innervate submucosa and villi. (v–vi) Terminal expression from stomach-innervating CG neurons (CG^{Stom}).

(D) The retrograde construct AAVrg-EGFP was injected into CG of GLP1R-Cre×Ai9 mice for mapping (IFN) ileal neurons, and the overlap between GFP+ and mCherry+ (GLP1R+) neurons was assessed (left). IFNs invariably expressed GLP-1R (middle). IFNs account for ~13% of ileal GLP-1R+ cells. No IFN+/GLP-1R-cell was detected (right).

(E) IFNs are enriched in Glp-1r RNA expression compared with myenteric neurons not projecting to CG, paired t test, $T(8) = 9.861$, * $p = 0.001$.

(F) AAVrg-EGFP-Cre was injected into CG of iDTR knock-in mice to ablate IFNs upon injecting diphtheria toxin (DTx) in the ileum. IFN ablation abolishes gastric enlargement by GLP-1^{ii}; stomach volumes 2-sample t test $T(8) = 7.821$, * $p < 0.001$.

(G) IFN ablation abolishes anorexia by GLP-1^{ii}; 1 h-food intake, two-way mixed RM-ANOVA, infusate × group: $F(2,16) = 11.148$,* $p = 0.001$.

(H) IFN ablation depleted myenteric GLP-1R+ neurons in the ileum; no expression detected in the myenteric jejunum; two-way mixed RM-ANOVA, intestinalsite × group $F(1,16) = 25.035$, * $p < 0.001$.

(H) IFN ablation abolishes CG Fos expression by GLP-1^{ii}; 2-sample t test $T(8) = 12.315$, * $p < 0.001$.

(J) AAVrg-Cre was injected into CG of wild-type (WT) mice followed by *Cre*-dependent AAVdj-DIO-Gs-mCherry into terminal ileum for chemogenetic activation of IFNs (IFN-Gs, controls injected with AAVdj-DIO-GFP, IFN-GFP). In a subgroup, AAV1-flex-Casp3 (controls with AAV1-DIO-EYFP) was used to locally ablate CG neurons.

(K) Chemogenetic IFN activation enhances CG Fos expression, 2-sample t test $T(8) = 8.485$, * $p < 0.001$.

(L) Chemogenetic IFN activation suppresses feeding, an effect abolished by CG ablation, 1 h-food intake, two-way mixed RM-ANOVA, infusate × group $F(2,34) = 7.193$, * $p = 0.002$.

(M) Same effects as in (L) but obtained with licks for lipid emulsion, $F(2,18) = 26.556$, * $p < 0.001$. Scale bars, 100 μM.
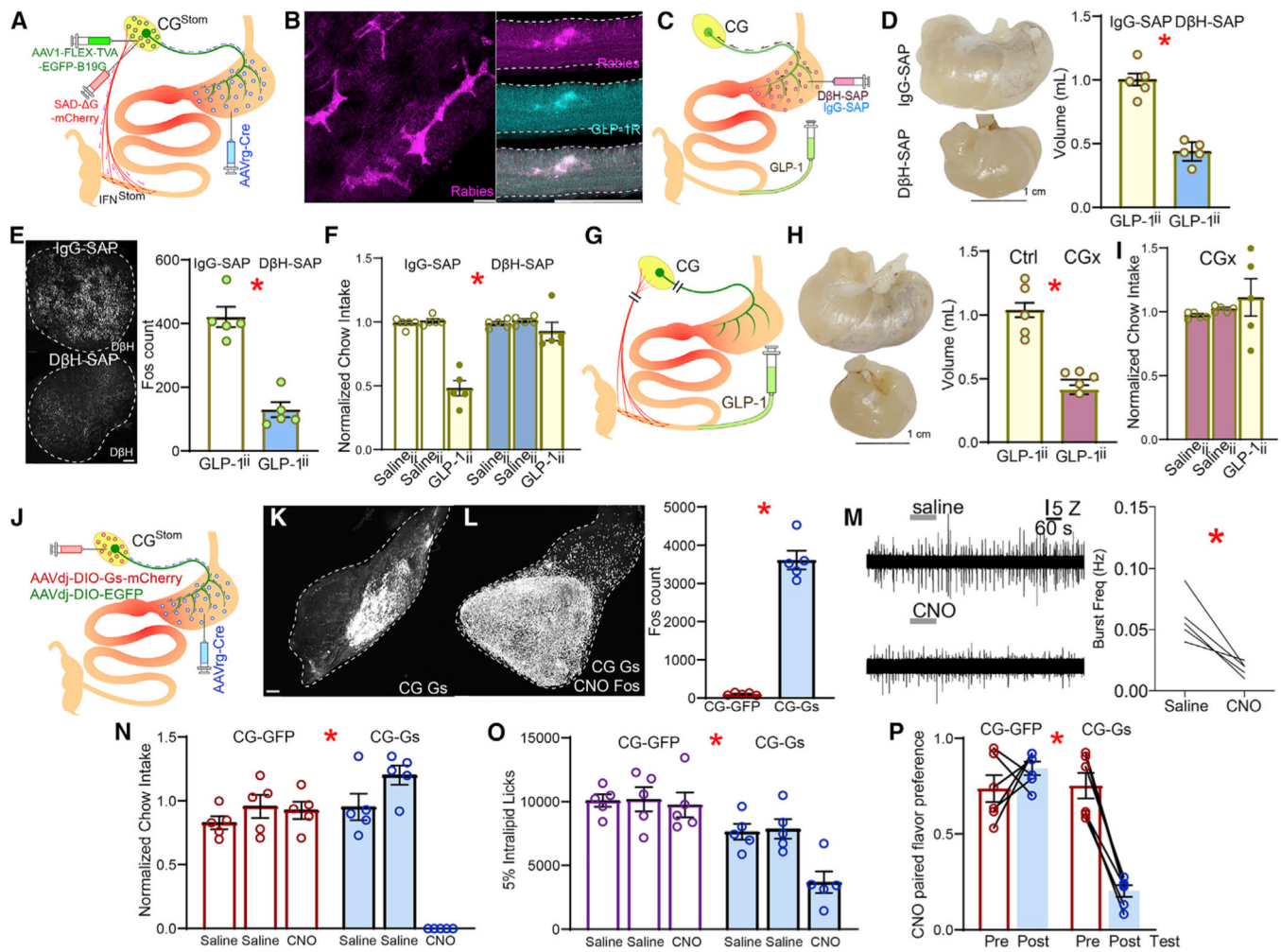
(N) Differential effects of intra-ileal or intra-duodenal infusions of methyl cellulose versus lipid on Fos expression in CG, with intra-ileal lipid infusions producing larger effects, two-way RM-ANOVA, infusate × intestinal site $F(1,16) = 5.630$, * $p = 0.031$.

(O) Intra-ileal and intra-duodenal lipid infusions produce similar effects on 1 h-food intake, two-way mixed RM-ANOVA, infusate × group $F(3,24) = 1.241$, * $p = 0.317$.

(P) However, intra-ileal caused slightly greater effects than intra-duodenal lipid infusions on active licking for lipid solutions, $F(3,24) = 5.787$, * $p = 0.004$. Data are represented as mean ± SEM in all figures.

See also Figure S2.

Figure 3. Intestinofugal neurons recruit stomach-innervating sympathetic neurons to mediate ileal GLP-1 effects

(A) Dysynaptic intestinofugal-to-stomach circuit mapped via cell-specific rabies viruses. First, the retrograde *Cre*-carrying construct AAVrg-Cre was injected into the stomach, concomitant to CG injections of the construct AAV1-synP-FLEX-splitTVA-EGFP-B19G. Then *Cre*-dependent, monosynaptic rabies SAD-ΔG-GFP was injected for replication within stomach-innervating CG neurons (CG^{Stom}). Tissues were then screened for rabies+ ileal IFNs synapsing onto CG^{Stom} (IFN^{Stom}).

(B) Rabies+ IFN^{Stom} were detected throughout the ileal myenteric layer and invariably expressed GLP-1Rs.

(C) Ablation of sympathetic CG^{Stom} by targeting the stomach with the retrograde immunotoxin anti-DβH-saporin (DβH-sap). Controls injected with mouse IgG-SAP.

(D) Gastric DβH-sap injections abolished stomach distension induced by GLP-1^{ii}; 2-sample t test T(8) = 6.566, * p < 0.001.

(E) In CG, DβH-sap ablated sympathetic neurons (left, anti-DβH immunolabeling) and abolished Fos induced by GLP-1^{ii} (right, T[8] = 7.257, * p < 0.001).

(F) Gastric DβH-sap abolished anorexia induced by GLP-1^{ii}, two-way mixed RM-ANOVA, infusate × group F(2,16) = 19.267, * p < 0.001.

(G) Celiactomies (CGx) were employed to assess GLP-1[ii] mechanisms.

(H) CGx abolished gastric enlargement induced by GLP-1[ii], 2-sample t test T(8) = 9.442, * p < 0.001.

(I) CGx abolished anorexia induced by GLP-1[ii], one-way RM-ANOVA, F(2,8) = 0.686, p < 0.531.

(J) AAVrg-Cre was injected into the stomach of WT mice followed by *Cre*-dependent AAVdj-DIO-Gs-mCherry into CG for chemogenetic activation of CG[Stom] (CG-Gs, controls injected with AAVdj-DIO-GFP, CG-GFP).

(K) mCherry expression in CG.

(L) CNO activation of CG[Stom] induces Fos in CG, CG-Gs versus CG-GFP T(8) = 14.204, * p < 0.001.

(M) CNO activation of CG-projecting IFNs reduces gastric contractions. Left: representative traces of stomach EMG recordings obtained from proximal gastric antrum following infusion of saline or CNO. Right: aggregate data of average frequency of EMG bursts. Paired t test T(4) = 4.627, * p = 0.009.

(N) Chemogenetic activation of CG[Stom] suppresses eating over 1 h; two-way mixed RM-ANOVA, injection × group F(2,16) = 57.494, * p < 0.001.

(O) Same effects obtained with licks for lipid solutions, F(2,16) = 4.900, * p = 0.022.

(P) Chemogenetic activation of CG[Stom] induces robust flavor aversion, F(1,10) = 34.913, * p < 0.001. Data are represented as mean ± SEM in all figures. Scale bars, 100 μM.

See also Figure S3.
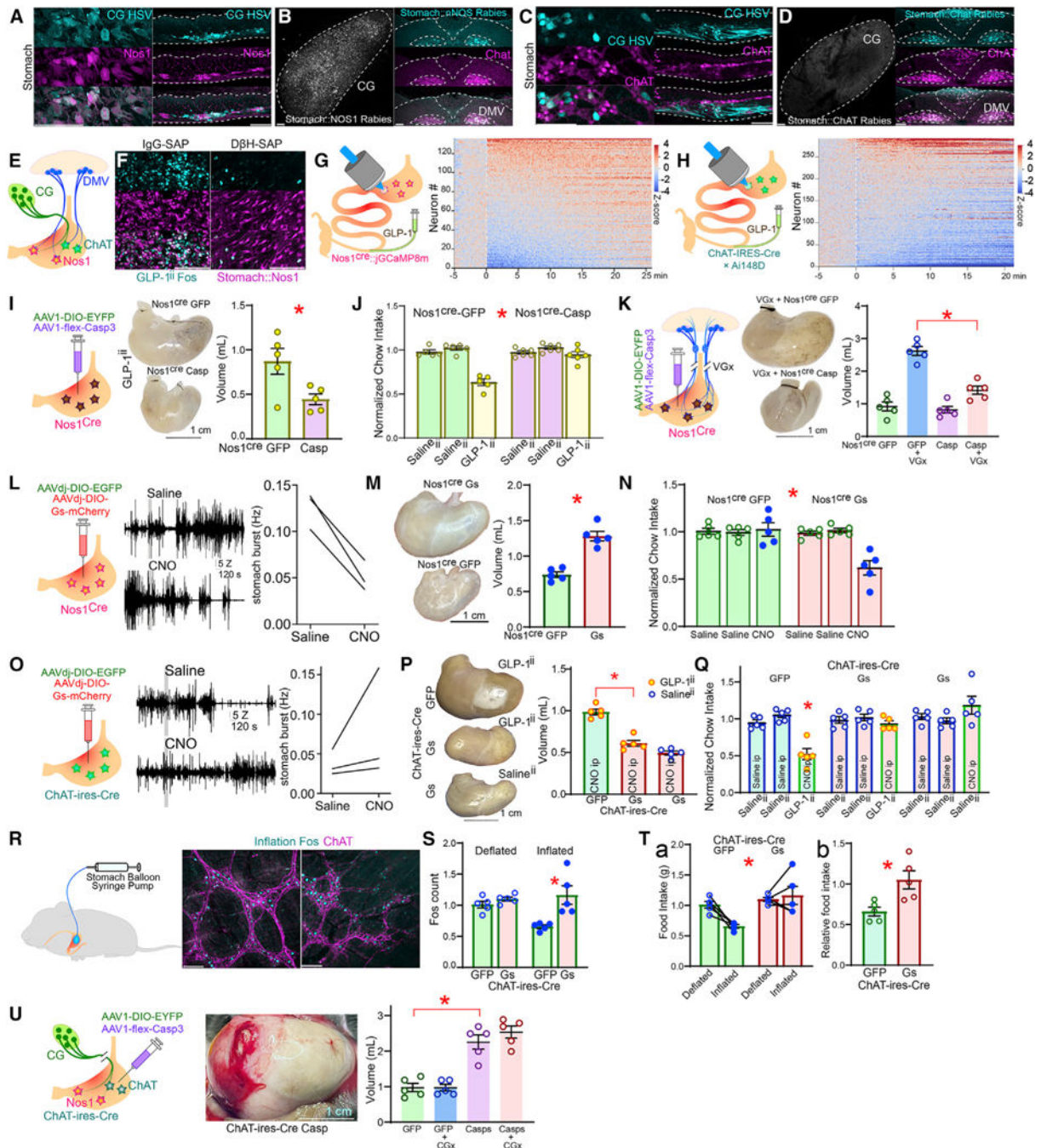
Figure 4. Abdominal sympathetic ganglia recruit Nos1+ gastric neurons to mediate ileal GLP-1 effects

(A) After gastric infections with the retrograde construct AAVrg-Cre, the polysynaptic, *Cre*-dependent anterograde *HSV* strain HSV-LSL-TK-Tomato was injected into CG. Recombination of HSV-LSL-TK-Tomato in CG^{Stom} reveals that CG preferentially targets Nos1+ (Nos1^{Stom}) gastric neurons.

(B) *Cre*-dependent rabies constructs injected into the stomach of Nos1^{Cre} mice labels CG^{Stom} and parasympathetic dorsal motor vagal (DMV) neurons.

(C) HSV-LSL-TK-Tomato recombining in CG^{Stom} reveals that CG does not target ChAT-gastric neurons (ChAT^{Stom}).

(D) *Cre*-dependent rabies constructs injected into the stomach of ChAT-ires-*Cre mice* labels DMV neurons but not CG^{Stom}.

(E) Whereas sympathetic CG^{Stom} innervates only Nos1^{Stom}, DMV innervates both Nos1^{Stom} and ChAT^{Stom}.

(F) GLP-1^{ii}-induced strong and specific Fos in Nos1^{Stom}, an effect abolished by DβH-sap.

(G) Left: injections of the *Cre*-dependent construct AAV9-syn-FLEX-jGCaMP8m into the stomach of Nos1^{Cre} mice allowed the expression of the genetic calcium sensor GCaMP6f specifically in Nos1^{Stom}. Right: upon implanting the abdominal glass window, intravital imaging revealed that GLP-1^{ii} induces fast and sustained calcium transients in Nos1^{Stom}. Heatmap of Z scores calculated with respect to baseline. T = 0 min: GLP-1^{ii} infusion.

(H) Much less pronounced effects were observed upon similar imaging of ChAT^{Stom} in ChAT-ires-Cre×Ai148D mice.

(I) Cell-specific ablation (AAV1-flex-Casp3) of Nos1^{Stom} abolishes GLP-1^{ii}-induced gastric expansion, T(8) = 2.709,* p = 0.027.

(J) Same effects for GLP-1^{ii}-induced appetite suppression, two-way mixed RM-ANOVA, infusate × group F(2,18) = 18.790,* p < 0.001.

(K) Cell-specific ablation of Nos1^{Stom} abolishes truncal vagotomy (VGx)-induced gastric bloating, one-way ANOVA F(3,16) = 43.610, p < 0.001; AAV1-DIO-EYFP+VGx versus AAV1-flex-Casp3+VGx Bonferroni * p < 0.001.

(L) Chemogenetic activation of Nos1^{Stom} (Nos1-Gs). Left: representative traces of EMG activity from stomach corpus following either saline (top trace) or CNO (lower trace). Blue insert traces show 1 s EMG, individual spikes shown were counted for plots. Right: aggregate data, average frequency EMG spikes, 20 min following saline or CNO, paired t test T(2) = 8.164, * p = 0.014.

(M) Chemogenetic Nos1^{Stom} activation induces marked stomach distension. Left: representative dissected stomachs; Right: volume of dissected stomachs, 2-sample t test T(8) = 6.960, * p < 0.001.

(N) Chemogenetic Nos1^{Stom} activation reduces 1 h-food intake in Nos1-Gs but not Nos1-GFP, two-way mixed RM-ANOVA, infusate × group F(2,16) = 10.806, * p = 0.001.

(O) Same as (M) and (N) but for chemogenetic activation of ChAT^{Stom} in ChAT-ires-*Cre* mice. CNO tended to increase frequency although effect was not significant, T(2) = 0.463, * p = 0.688.

(P) Chemogenetic activation of ChAT^{Stom} abolishes GLP-1^{ii}-induced gastric bloating, one-way RM-ANOVA, F(2,12) = 66.773, p < 0.001, ChAT-Gs(GLP-1^{ii}) versus ChAT-GFP(GLP-1^{ii}) Bonferroni * p < 0.001.

(Q) Chemogenetic activation of ChAT^{Stom} abolishes GLP-1^{ii}-induced anorexia, two-way mixed RM-ANOVA, treatment (Saline^{ii} versus GLP-1^{ii}) × group F(2,24) = 9.704, p < 0.001; ChAT-Gs(GLP-1^{ii}) versus ChAT-GFP(GLP-1^{ii}) Bonferroni *p = 0.014.

(R–S) Gastric balloon inflation induces Fos in ChAT^{Stom}, one-way RM-ANOVA, F(3,16) = 7.521, p = 0.002, inflated-GFP versus inflated-Gs, Bonferroni * p = 0.003.

(T) ChAT^{Stom} activation entirely abolished gastric balloon-induced anorexia, (Ta) Chow intake: two-way mixed RM-ANOVA, inflation 3 group F(1,8)= 8.160, * p = 0.021, and

group effect $F(1,8) = 10.761$, ** $p = 0.011$. (Tb) Normalized intake reduction upon balloon inflation, $T(8) = 3.172$, * $p = 0.013$.

(U) Cell-specific ablation (AAV1-flex-Casp3) of ChAT**Stom** causes extreme gastric bloating irrespective of CGx, one-way ANOVA $F(3,16) = 30.119$, * $p < 0.001$, AAV1-flex-Casp3 versus AAV1-DIO-EYFP Bonferroni * $p < 0.001$. Data are represented as mean ± SEM in all figures. Scale bars, 100 μM.

See also Figure S4 and Video S1.
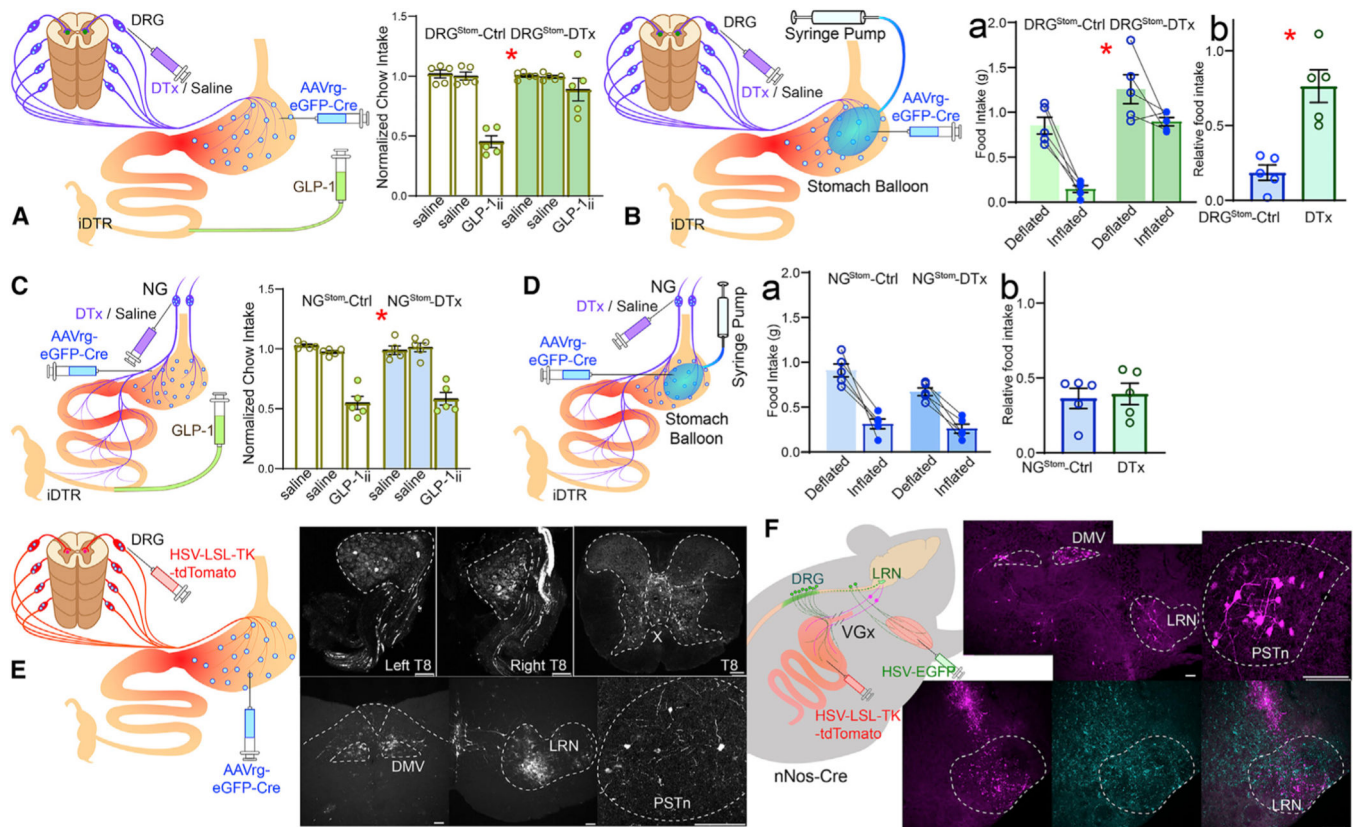
Figure 5. Stomach-innervating spinal sensory neurons convey gastric distention signals induced by ileal GLP-1

(A) Ablation of stomach-innervating DRGs (DRG^{Stom}). Retrograde *Cre*-expressing AAVrg-Cre was injected into the stomach of iDTR mice, followed by intrathecal infusions of diphtheria toxin (DTx). DRG^{Stom} ablation abolished GLP-1^{ii}-induced anorexia, two-way mixed RM-ANOVA, infusate F(2,16) = 29.592, * p < 0.001, group F(1,8) = 17.513, *p = 0.003, infusate × group F(2,16) = 13.117, *p < 0.001.

(B) DRG^{Stom} ablation significantly attenuated gastric balloon-induced anorexia. (Ba) Chow intake: two-way mixed RM-ANOVA, inflation × group F(1,8) = 2.725, p = 0.137, main effects of balloon F(1,8) = 26.270, *p < 0.001 and group F(1,8) = 39.166, **p < 0.001. (Bb) Normalized intake reduction upon balloon inflation, T(8) = 4.788, *p = 0.001.

(C and D) As in (A) and (B) but ablation of stomach-innervating NGs (NG^{Stom}). NG^{Stom} ablation failed to affect either GLP-1^{ii}-induced (C, two-way mixed RM-ANOVA infusate × group F[2,16] = 0.557, p = 0.583), or balloon-induced (Da, two-way mixed RM-ANOVA, inflation 3 group F[1,8] = 2.262, p = 0.171; Db, T[8] = 0.304, p = 0.769) anorexia.

(E) HSV-LSL-TK-Tomato bilaterally injected into DRG^{Stom} (T7–T10) revealed robust recombination in thoracic DRGs (note labeled sensory fibers), spinal cord (note labeled neurons inviscera-related Rexed laminaX), DMV, sensory medullary lateral reticular nucleus (LRN), and parasubthalamicnucleus of the hypothalamus (PSTn).

(F) In VGx mice, HSV-LSL-TK-Tomato injected into the stomach of Nos1^{Cre} mice labeled DMV, LRN, and PSTn. The stomach-recipient LRN field partially overlapped with
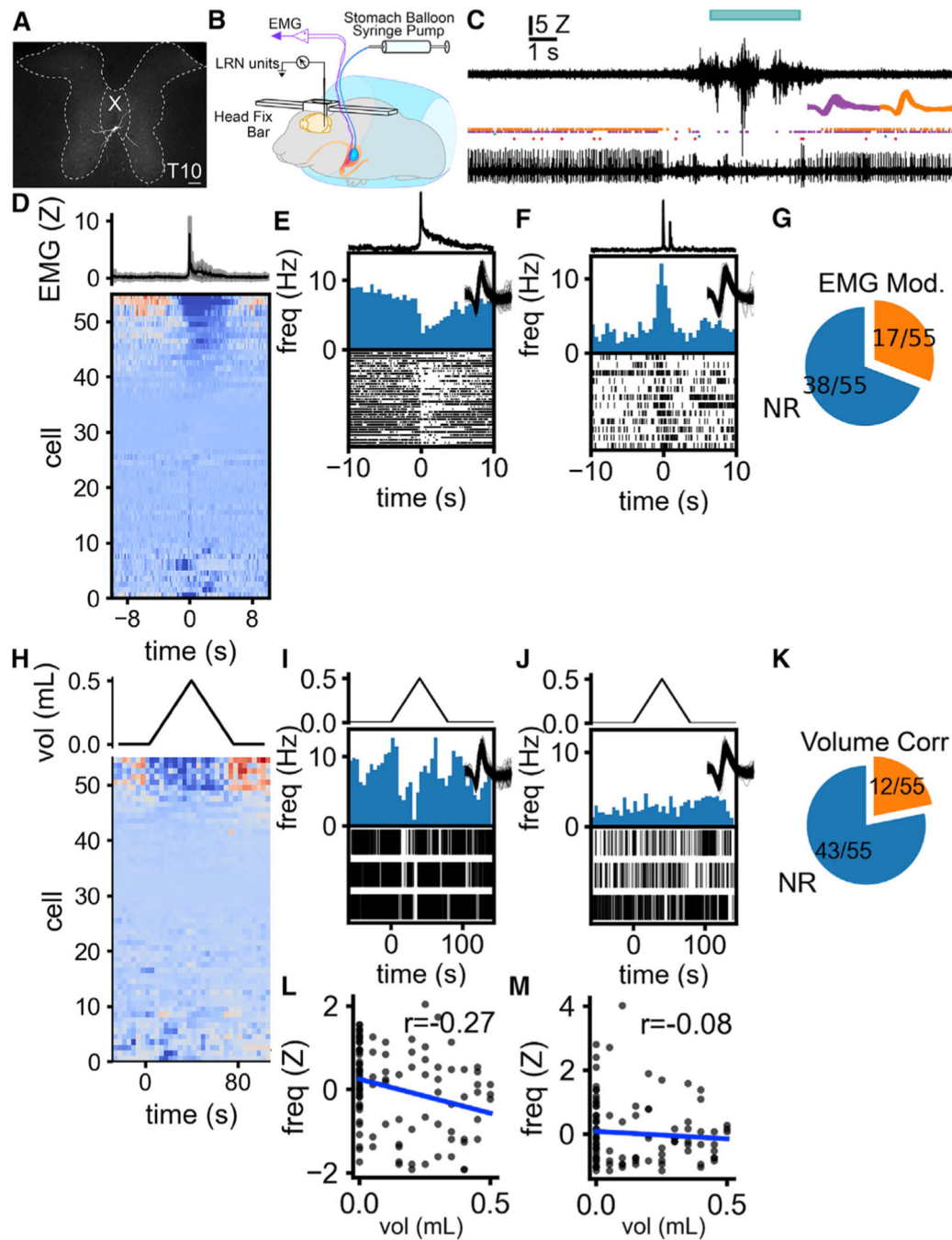
the forelimb-recipient LRN field defined by forelimb injections of HSV-EGFP. Data are represented as mean ± SEM in all figures. Scale bars, 100 μM.

See also Figure S5 and Table S1.

Figure 6. Single neurons in the lateral reticular nucleus detect gastric contractions

(A) *Cre*-dependent rabies injections in LRN of VGlut1-*ires-Cre* mice show that LRN[VGlut1] neurons are innervated by large thoracic spinal cord *lamina X* neurons.

(B) Single neuron activity in LRN and gastric EMG synchronously recorded during intra-gastric balloon inflation in head-fixed, awake mice.

(C) Representative traces of EMG and single-unit activity. Top trace, stomach EMG. The cyan bar above the EMG indicates the detection of a contraction. Rasters, each tick indicates the occurrence of a spike from a discriminated unit at the recording site. Two units are

presented in purple and orange. Bottom trace, activity from the recording site from which rasters were constructed.Inset traces, waveforms of sorted units.

(D–F) LRN cells are modulated in concert with stomach contraction. (D) LRN cell activity aligned with the initiation of a stomach contraction. The top trace is a triggered average of EMG activity. (E) The representative individual unit that is inhibited during stomach contraction. The top line plot shows the burst-triggered EMG from the stomach. The lower histogram and raster show the change in unit activity aligned to the onset of individual contractions. (F) Representative individual unit excited during stomach contraction.

(G) The proportion of single units showing significant changes in firing rate in response to stomach contractions. 17/55 cells showed a significant change in firing rate between these periods.

(H–J) Some LRN cells are inhibited during stomach distension. (H) LRN cell activity aligned to a programmed sequence of inflation then deflation of a balloon implanted in the stomach. The top line plot shows the volume of the stomach balloon. (I) The single unit that is negatively correlated with the balloon volume, same cell as (E). The top line shows balloon volume. Lower histogram and raster show changes in unit activity during balloon inflation and deflation. (J) The single unit that has no correlation with balloon volume, same cell as (F).

(K) The proportion of single units that show a significant correlation with balloon volume. 12 cells showed significant correlations between firing rate and balloon volume.

(L) Example of the correlation between balloon volume and firing rate for the unit shown in (E) and (I) (r = −0.27, p = 0.0059).

(M) Example of the correlation between balloon volume and firing rate for the unit shown in (F) and (J) (r = −0.078, p = 0.43). Scale bars, 100 μM.

See also Figure S6.
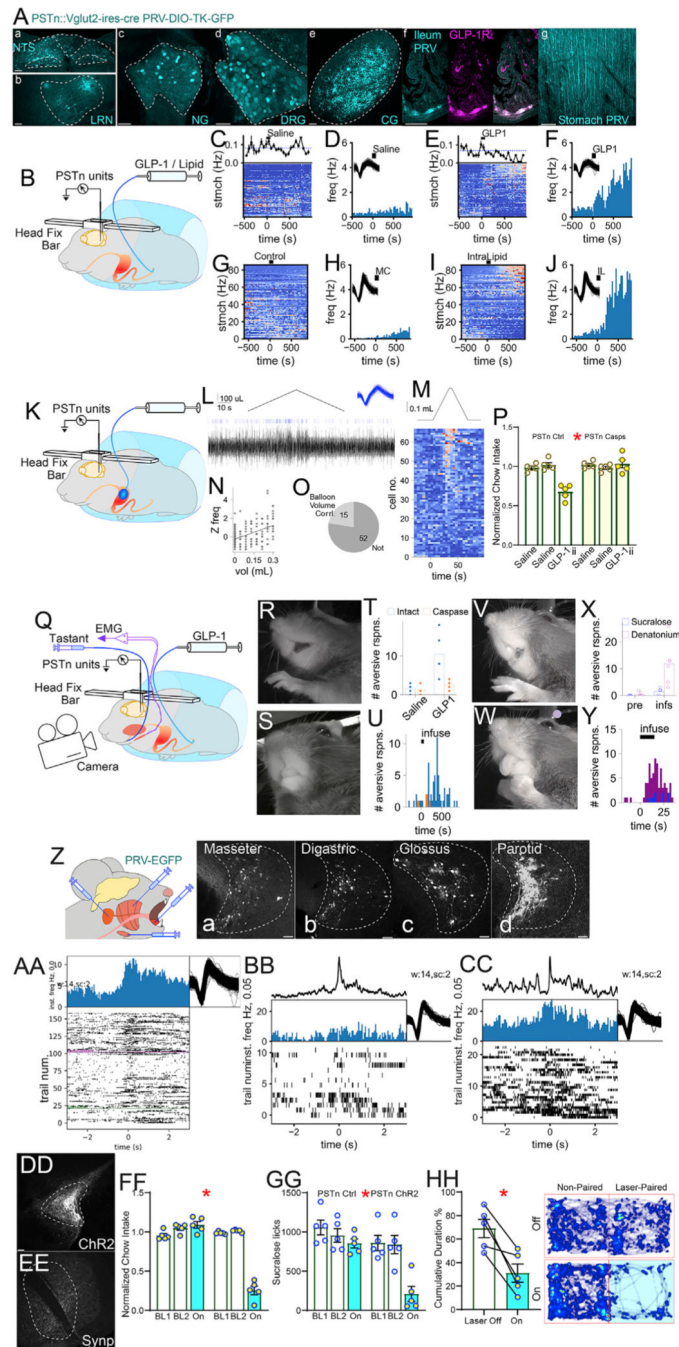
Figure 7. Parasubthalamic neurons encode for gastric distension, respond to ileal stimulation, and mediate craniofacial motor responses to ileal GLP-1

(A) Injection of retrograde *Cre*-dependent PRV-DIO-TK-GFP into PSTn of VGlut2-ires-Cre mice labeled *nucleus tractus solitarius* (NTS) (a), LRN (b), NG (c), thoracic DRGs (d), CG (e), and ileal GLP-1R+ myenteric neurons (f). Note passing fibers across stomach wall (g).

(B) Single neuron activity in PSTn of head-fixed awakemice recorded during intra-ileal infusions of GLP-1 (GLP-1ii) or lipid (Lipidii).

(C) Upper line plot: frequency of stomach contraction bursts over time. The dotted blue line shows the average baseline rate for the timepoints before infusion of saline. Heatmap: Z-transformed firing rates from 76 PSTn cells (one neuron/line). Activity from each recorded cell was aligned to the infusion of a control solution into the ileum at time zero.

(D) Binned firing rate of a neuron's responses to control (Saline[ii]).

(E) Upper plot: as in (C), but for GLP1[ii]. Heatmap: as in

(C) but aligned to 30 pmol/kg GLP1[ii] at time zero. Cells ranked according to responsiveness to GLP-1[ii].

(F) Binned firing rate of the neuron shown in (D) in response to GLP1[ii]. Note ~5-fold increase compared with Saline[ii].

(G) As in (C), but for ileal methylcellulose (MC, volume control). Heatmap: Z-transformed firing rates from 86 PSTn cells.

(H) Binned firing rate of a cell's responses to a control infusion of MC.

(I) Heatmap aligned to infusion of 200 μL IntraLipid into the ileum (Lipid[ii]) at time zero. The same cells are shown in the same row order as (G), with the same color mapping. Cells ranked according to responsivenss to Lipid[ii].

(J) Binned firing rate of the neuron shown in (H) in responseto Lipid1[ii]. Note ~5-fold increase compared with MC.

(K) Single neuron activity in PSTn of head-fixed awake mice recorded during intra-gastric balloon inflation/deflation.

(L) Example trace of a unit activated by stomach distension. The black chevron above shows the volume of the balloon, blue ticks are spikes for an isolated unit, and black trace below is activity at the recording site from which spikes were sorted. Blue inset are overlayed waveforms from each sorted spike.

(M) Chevron above represents balloon volume. Heatmapshows Z-transform of time-binned firing frequency of 67 PSTn neurons recorded in 6 sessions from 4 animals. For each neuron, responses to at least 3 balloon inflation trials were averaged. Heatmap lines ranked according to responsiveness to balloon inflation.

(N) Correlation of PSTn neuronal activity with balloon volume. Top: unit depicted in (L) is significantly correlated with balloon volume (Z-transform frequency versus balloon volume).

(O) 15/67 PSTn neurons display a significant correlationwith balloon volume.

(P) Cell-specific ablation (AAV5-flex-Casp3) of VGlut2+ PSTn neurons (PSTn[VGlut2]) abolishes GLP-1[ii]-induced anorexia, two-way mixed RM-ANOVA, infusate $\times$ group $F_{(2,16)} = 20.444,^*$ $p < 0.001$.

(Q) Single neuron activity in PSTn of awake head-fixedmice recorded during either ileal infusions of GLP-1 (GLP-1[ii]) or intra-oral infusions of tastants. Concomitantly, electromyogram activity was recorded from the masseter and digastric jaw muscles, while a high-res camera imaged taste reactivity.

(R) The representative frame of rejection-like reactivity (gaping) to GLP-1[ii], in an intact animal.

(S) Representative frame of indeterminate (neutral) response to GLP-1[ii] in an animal sustaining PSTn[VGlut2] ablations.

(T) Intact animals (n = 5) displayed significantly more rejection-like responses following GLP-1[ii] compared with animals sustaining PSTn[VGlut2] ablations (n = 4); t test T(7) = 2.752, * p = 0.028.

(U) Rejection-like responses are displayed within ~5–10 min of GLP-1[ii] (n = 5). Responses binned into 30-s epochs following GLP-1[ii] at t = 0.

(V and W) Representative frames of orofacial reactivity to intra-oral infusions bitter (denatonium, gaping, V) and sweet (sucralose, tongue protrusion, W) tastes in intact animals.

(X) Bitter taste evoked more rejection-like responses than sweet taste. Paired t test T(5) = 2.97, p = 0.031.

(Y) Rejection-like responses to tastes are observed within seconds of oral infusions.

(Z) Polysynaptic retrograde PRV-CMV-EGFP was injected into either masseter (Za), digastric (jaw muscles) (Zb), genioglossus (*Glossus*, an extrinsic muscle of the tongue that mediates tongue protrusion) (Zc), or parotid salivary gland (Zd). All injections yielded labeling in PSTn.

(AA) Initiation of electromyographic contractions of digastric muscle is used to construct a raster plot of a PSTn unit. The neuron's firing rate increases as the digastric muscle activates. Trials, digastric contractions.

(BB) Raster triggered by bursts of activity in the digastric muscle following infusions of sucralose. The trace above the histogram shows the averaged digastric EMG waveform.

(CC) Raster triggered by on bursts of activity in the digastric muscle elicited by infusions of denatonium.

(DD) *Cre*-dependent channelrhodopsin2 (AAV5-DIO-hChR2-EYFP, controls AAV5-DIO-EYFP) was injected into PSTn[VGlut2] for cell type-specific optogenetic manipulation.

(EE) *Cre*-dependent synaptophysin (AAV5-hSyn-FLEx-mGFP-Synaptophysin-mRuby) into PSTn[VGlut2] neurons results in dense terminal labeling in the ipsilateral pontine parvocellular reticular formation (PCRt), a region containing premotor circuits that control masseter and digastric motor trigeminal neurons.

(FF) Bilateral optogenetic activation of PSTn[VGlut2] terminals in PCRt (PSTn[VGlut2]→PCRt) strongly inhibited 1 h-food intake, two-way mixed RM-ANOVA, laser × group F(2,16) = 102.980, *p < 0.001.

(GG) Similar effects obtained during laser pulses triggered by licks to the artificial sweetener sucralose, F(2,16) = 17.573, *p < 0.001.

(HH) PSTn[VGlut2]/PCRt optical activation induces strong place avoidance during online laser-conditioned place preference tests paired t test T(4) = 4.493,*p = 0.011. Data are represented as mean ± SEM in all figures. Scale bars, 100 μM.

See also Figure S7, Table S1, and Videos S2 and S3.

KEY RESOURCES TABLE

REAGENT or RESOURCE	SOURCE	IDENTIFIER
Antibodies		
Rabbit-anti-mCherry	Abcam	Cat# ab167453 RRID: AB_2571870
Rabbit-anti-c-Fos	Abcam	Cat# ab190289 RRID: AB_2737414
Goat polyclonal anti c-Fos	Abcam	Cat# ab156802 RRID:AB_2747692
Goat Anti-GFP antibody (FITC)	Abcam	Cat# ab6662 RRID: AB_305635
FITC Anti-Biotin antibody	Abcam	Cat# ab53469 RRID:AB_867862
Rabbit-anti-GLP-1 R	Abcam	Cat# ab218532 RRID: AB_2864762
Rabbit-anti-GLP1	Abcam	Cat# ab22625 RRID: AB_447206
Goat-anti-ChAT	Millipore	Cat# AB144 RRID: AB_90650
Rabbit Anti-DBH	Abcam	Cat# ab209487 RRID: AB_2892178
Goat Anti-Nos1	Abcam	Cat# ab1376 RRID: AB_300614
Rabbit Anti-NeuN (Alexa647)	Abcam	Cat# ab190565 RRID:AB_2732785
Alexa Fluor® 594 AffiniPure Donkey Anti-Rabbit IgG	Jackson Immuno Research Labs	Cat# 711–585-152 RRID:AB_2340621
TRITC-conjugated affinipure Goat anti-Rabbit IgG (H+L)	Jackson Immuno Research Labs	Cat# 111–025-144 RRID: AB_2337932
FITC-conjugated affinipure goat anti-rabbit IgG (H+L)	Jackson Immuno Research Labs	Cat# 111–095-144 RRID: AB_2337978
FITC-conjugated affinipure Donkey AntiGoat IgG (H+L)	Jackson Immuno Research Labs	Cat# 705–095-147 RRID: AB_2340401
TRITC-conjugated affinipure Donkey AntiGoat IgG (H+L)	Jackson Immuno Research Labs	Cat# 705–025-147 RRID: AB_2340389
Biotinylated Goat Anti-Rabbit IgG antibody	Vector Laboratories	Cat# BA-1000 RRID: AB_2313606
Chemicals, peptides, and recombinant proteins		
CCK-SAP	Advanced Targeting Systems	Cat # IT-31
Blank-SAP	Advanced Targeting Systems	Cat# IT-21
Anti-DBH-SAP	Advanced Targeting Systems	Cat # IT-03
Mouse IgG-SAP	Advanced Targeting Systems	Cat# IT-18
FluoroGold (FG)	Fisher scientific	Cat# NC0560981
CCK8	AnaSpec	Cat # AS-20739
GLP-1 (7–36)	AnaSpec	Cat # AS-22462
Biotin-labeled GLP-1 (7–36)	AnaSpec	Cat # AS-23586
Exendin-9, Exendin (9–39)	AnaSpec	Cat # AS-24467
Exendin-4	AnaSpec	Cat # AS-24463
FAM-labeled Exendin-4	AnaSpec	Cat # AS-60280–05
Intralipid 20%, emulsion	SigmaAldrich	Cat# I141
Cellulose	SigmaAldrich	Cat # 435236–250G
Diphtheria Toxin	SigmaAldrich	Cat # D0564–1 MG
IntraLipid 20%, emulsion	SigmaAldrich	Cat# I141–100ML
Sucralose	SigmaAldrich	Cat # 69293–100G
Clozapine N-oxide (CNO)	Enzo Life Sciences	Cat # BML-NS105–0025
Cholic Acid	Alfa Aesar	Cat # A11257
Hoechst 33342	Invitrogen	Cat # H3570

REAGENT or RESOURCE	SOURCE	IDENTIFIER
Critical commercial assays		
VECTASTAIN Elite ABC HRP Kit (Peroxidase, Standard)	Vector Laboratories	Cat# PK-6100
Experimental models: Organisms/strains		
Mouse: C57BL/6J (B6)	The Jackson Laboratory	JAX: 000664
Mouse: $Glp1r^{tm1.1(cre)Lbrl}$/RcngJ (Glp1r-ires-Cre)	The Jackson Laboratory	JAX: 029283
Mouse: B6; 129S-$Gcg^{tm1.1(icre)Gkg}$/J (Gcg^{iCre})	The Jackson Laboratory	JAX:030663
Mouse: B6.Cg-Gt(ROSA) $26Sor^{tm32CAG-COP4*H134R/EYFP)Hze}$/J (Ai32)	The Jackson Laboratory	JAX: 024109
Mouse: B6N;129-Tg(CAG-CHRM3*,-mCi-trine)1Ute/J (CAG-LSL-Gq-DREADD)	The Jackson Laboratory	JAX: 026220
Mouse: $Slc17a6^{tm2(cre)Lowl}$/J (Vglut2-ires-cre)	The Jackson Laboratory	JAX: 016963
Mouse: B6;129S-$Slc17a7^{tm1.1(cre;Hze}$/J (Vglut1-IRES2-Cre-D)	The Jackson Laboratory	JAX:023527
Mouse: C57BL/6-Gt(ROSA) $26Sor^{tm1(HBEGF)Awai}$/J (B6-iDTR)	The Jackson Laboratory	JAX:007900
Mouse: B6.129S-Chat$^{tm1(cre)Lowl}$/MwarJ (B6J.ChAT-IRES-Cre:: neo)	The Jackson Laboratory	JAX: 031661
Mouse: B6.129-$Nos1^{tm1(cre)Mgmj}$/J (Nos1^{cre})	The Jackson Laboratory	JAX: 017526
Mouse: B6.Cg-Gt(ROSA) $26Sor^{tm9(CAG-tdTomato)Hze}$/J (Ai9)	The Jackson Laboratory	JAX:007909
Mouse: B6.Cg-$Igs7^{tm148.1(tetO-GCaMP6f,CAG-tTA2)Hze}$/J (Ai148D)	The Jackson Laboratory	JAX: 030328
Mouse: B6.;129-Gt(ROSA) $26Sor^{tm5(CAG-Sun1/sfGFP)Nat}$/J (CAG-Sun1/sfGFP)	The Jackson Laboratory	JAX: 021039
Recombinant DNA		
AAV2-retro.hSyn.Cre	Dr. Wilson-Addgene AAV Viral Service	Addgene Viral Prep: 105553-AAVrg
AAV2-retro-hSyn.HI.EGFP-Cre	Dr. Wilson-Addgene AAV Viral Service	Addgene Viral Prep: 105540-AAVrg
AAV2-retro-hSyn-EGFP	Dr. Roth-Addgene AAV Viral Service	Addgene Viral Prep: 50465-AAVrg
AAV1 hSyn FLEx mGFP-2A-Synaptophysin-mRuby	Dr. Luo-Addgene AAV Viral Service	Addgene Viral Prep: 71760-AAV1
AAV1-synP-FLEX-splitTVA-EGFP-B19G	Dr. Wickersham-Addgene AAV Viral Service	Addgene Viral Prep: 52473-AAV1
AAV5-EF1a-DIO-hChR2(H134R)-EYFP	Dr. Deisseroth-Addgene AAV Viral Service	Addgene Viral Prep:20298-AAV5
AAV1/AAV5-Ef1a-DIO-EYFP	Dr. Deisseroth-Addgene AAV Viral Service	Addgene Viral Prep:27056-AAV5
AAV1-syn-FLEX-jGCaMP8m	GENIE Project Lab-Addgene AAV Viral Service	Addgene Viral Prep:162378-AAV1
AAV-DJ-hSyn-DIO-rM3D(Gs)-mCherry	Dr. Roth - Duke Viral Vector Core	Addgene Plasmids: 50458
AAV-DJ-hSyn-DIO-hM4D(Gi)-mCherry	Dr. Roth - Duke Viral Vector Core	Addgene Plasmids: 44362
AAV-DJ-hSyn-DIO-mCherry	Dr. Roth - Duke Viral Vector Core	Addgene Plasmids: 50459

REAGENT or RESOURCE	SOURCE	IDENTIFIER
AAV-DJ-hSyn-DIO-EGFP	Dr. Roth - Duke Viral Vector Core	Addgene Plasmids: 50457
AAV1 /AAV5-flex-taCasp3-TEVp	Dr. Shah - University of North Carolina's Vector Core	Addgene Plasmids: 45580
H129 CAG-LSL-TK-tdTomato	NIH Center for Neuroanatomy with Neurotropic Virus	TK-TT
H129 CMV-EGFP	NIH Center for Neuroanatomy with Neurotropic Virus	414
PRV CAG-DIO-TK-GFP	NIH Center for Neuroanatomy with Neurotropic Virus	Ba-2017
PRV CMV-EGFP	NIH Center for Neuroanatomy with Neurotropic Virus	152
EnvA G-Deleted Rabies-mCherry	Viral Vector Core - Salk Institute for Biological Studies	32636
EnvA G-Deleted Rabies-eGFP	Viral Vector Core - Salk Institute for Biological Studies	32635
Deposited data		
Behavioral, electrophysiological, anatomy, and analyzed intravital imaging rare data	Mendeley Data.com	https://doi.org/10.17632/zkjm36wp8s.1
Software and algorithms		
Matlab R20 17b	MathWorks	http://www.mathworks.com/products/matlab/
PatchMaster 2.20	HEKA	http://www.heka.com/index.html
Igor Pro 6.36	WaveMetrics	https://www.wavemetrics.com/
EthoVision XT 11.5	Noldus	http://www.noldus.com/animal-behavior-research/products/ethovision-xt
LabView 2014	LabView	http://www.ni.com/download/labview-development-system-2014/4735/en/
GraphPad Prism 9	GraphPad	http://www.graphpad.com/scientific-software/prism/
Adobe design standard CS6	Adobe	http://shop.adobe.com/
IBM SPSS statistics 24.0	IBM Predictive Software	https://www.ibm.com/support/knowledgecenter/SSLVMB
Win Movie Maker	VideoWinSoft Software	http://www.VideoWinSoft.com
Axograph X	AxoGraph	http://www.axograph.com
ImageJ	NIH	https://imagej.nih.gov/ij/
Python 3	Python Software Foundation.	https://www.python.org/
OpenCV 4.5.3	OpenCV team	https://opencv.org/
Ffmpeg n4.4	FFmpeg team	https://www.ffmpeg.org/
NoRMCorre: Non-Rigid Motion Correction	Pnevmatikakis and Giovannucci (2017)	https://github.com/flatironinstitute/NoRMCorre
CalmAn-MATLAB	Pnevmatikakis et al. (2016); Giovannucci etal. (2019)	https://github.com/flatironinstitute/CaImAn-MATLAB
Other		

REAGENT or RESOURCE	SOURCE	IDENTIFIER
Totally Light 2Go - non-caloric powdered flavor drink mix, cranberry and wild berry flavors; sugar-free, Splenda-sweetened	4C Foods Corp.	N/A
Implantable Optical Fibers	Doric Lenses, Canada	MFC_200/240–0.22_6mm_ZF1.25(G)_FLT
ICV Single Guide Cannula, 24 Gauge Stainless-Steel, Short Pedestal, Cut Length 6mm	P1 Technologies	Cat # C316GS
ICV Single Dummy Cannula, 24 Gauge Stainless-Steel, Fit On Cap	P1 Technologies	Cat # C316FD
ICV Single Internal Cannula, 31 Gauge Stainless-Steel, Short Pedestal	P1 Technologies	Cat # C316IS
Homeothermic Monitoring System	Harvard Apparatus	Cat # 55–7020
Nanofil Application Kits (Microinjection)	World Precision Instruments	Cat # Beveled (IO-KIT)
NanoFil Needles (Microinjection)	World Precision Instruments	Cat # Beveled, 36G (NF36BV-2)
Pump 11 Elite Nanomite (Microinjection)	Harvard Apparatus	Cat # 70–4507
Spinal Cord Hook (Vagal operation)	Fine Science Tools	Cat #10162–12
Double Ended Periosteal Elevator (Spinal operation)	GerVetUSA	Cat # GD50–1720
Mouse Spinal Adaptor (Spinal operation)	Stoelting	Cat #51690
Mouse Transverse Clamps (Spinal operation)	Stoelting	Cat #51691
Delicate Suture Tying Forceps (Microsurgery)	Fine Science Tools	Cat# 11063–07
Formvar-Insulated Nichrome Wires (EMG recording)	A-M system	Cat# 761000
Microwire connections (EMG recording)	Neuralynx	Cat # EIB-16
16 tungsten microwires, 35-μm diameter (Electrophysiological recordings)	TDT systems	Cat # OMN1005
Masterflex® Nylon, Female Luer (Fistula)	Cole-Parmer	Cat # UX-45502–20
Masterflex®, Polypropylene, Male Luer Lock (Fistula)	Cole-Parmer	Cat # EW-30800–30
Round Cover Slip German Glass #1.5, 15 mm (Intravital microscopy)	Electron Microscopy Sciences	Cat #64–0713
Ultra Gel Control Super Glue (Intravital window)	Loctite	Cat # 45208
Stainless steel large penny fender washers M12×24×1.5mm (Intravital microscopy)	Dywishkey	Cat # 304
Low Toxicity Silicone Adhesive (Intravital microscopy)	WPI	Cat # KWIK-SIL
FluoroDish Cell Culture Dish 50mm	WPI	Cat # FD5040–100
Catheter for mouse jugular vein, 1 to 3Fr, 10.5cm, collar @1.2cm. Fits 22ga. (Gastric balloon)	Instech laboratories	Cat # C10PU-MJV1403
MicroRenathane tubing (OD 0.025") (Ileo catheterization)	Braintree Scientific	Cat # MRE025
Balloon Latex Balloon size 4 (0.06ML) (Gastric balloon)	Harvard Apparatus	Cat # PY2 73–3479
Silicon probes	Neuronexus	Cat # A2×2-tet-10mm-150–150-121-A16
Headplates	Mt. Sinai Machine Shop / https://neurophysics.ucsd.edu/lab_hardware.php	Rev 01 2011 Part A
Patch Clamp Amplifier	Molecular Devices	Cat # Multiclamp 700B
Confocal microscope	Leica	TCS SP8 STED 3X
Multiphoton microscope	Olympus	FVMPE-RS
Single Unit Recording Amp	TDT	RZ5
Digitizer and Sequencer	CED	Micro 1401
LED for slice illumination	Mightex	LCS-0470–50-22

REAGENT or RESOURCE	SOURCE	IDENTIFIER
Miltenyi Tyto microfluidic sorter	Miltenyi Biotec	Cat #130–103-931